Computational Mechanics (2019) 63:1165–1185
https://doi.org/10.1007/s00466-018-1642-1

ORIGINAL PAPER

Tire aerodynamics with actual tire geometry, road contact and tire deformation

Takashi Kuraishi[1] · Kenji Takizawa[1] · Tayfun E. Tezduyar[2,3]

Received: 9 July 2018 / Accepted: 2 October 2018 / Published online: 13 October 2018

Abstract
Tire aerodynamics with actual tire geometry, road contact and tire deformation pose tough computational challenges. The challenges include (1) the complexity of an actual tire geometry with longitudinal and transverse grooves, (2) the spin of the tire, (3) maintaining accurate representation of the boundary layers near the tire while being able to deal with the flow-domain topology change created by the road contact and tire deformation, and (4) the turbulent nature of the flow. A new space–time (ST) computational method, "ST-SI-TC-IGA," is enabling us to address these challenges. The core component of the ST-SI-TC-IGA is the ST Variational Multiscale (ST-VMS) method, and the other key components are the ST Slip Interface (ST-SI) and ST Topology Change (ST-TC) methods and the ST Isogeometric Analysis (ST-IGA). The VMS feature of the ST-VMS addresses the challenge created by the turbulent nature of the flow, the moving-mesh feature of the ST framework enables high-resolution flow computation near the moving fluid–solid interfaces, and the higher-order accuracy of the ST framework strengthens both features. The ST-SI enables moving-mesh computation with the tire spinning. The mesh covering the tire spins with it, and the SI between the spinning mesh and the rest of the mesh accurately connects the two sides of the solution. The ST-TC enables moving-mesh computation even with the TC created by the contact between the tire and the road. It deals with the contact while maintaining high-resolution flow representation near the tire. Integration of the ST-SI and ST-TC enables high-resolution representation even though parts of the SI are coinciding with the tire and road surfaces. It also enables dealing with the tire–road contact location change and contact sliding. By integrating the ST-IGA with the ST-SI and ST-TC, in addition to having a more accurate representation of the tire geometry and increased accuracy in the flow solution, the element density in the tire grooves and in the narrow spaces near the contact areas is kept at a reasonable level. We present computations with the ST-SI-TC-IGA and two models of flow around a rotating tire with road contact and prescribed deformation. One is a simple 2D model for verification purposes, and one is a 3D model with an actual tire geometry and a deformation pattern provided by the tire company. The computations show the effectiveness of the ST-SI-TC-IGA in tire aerodynamics.

Keywords Tire aerodynamics · Actual tire geometry · Road contact · ST Variational Multiscale method · ST Slip Interface method · ST Topology Change method · ST Isogeometric Analysis

1 Introduction

In this article, we address the computational challenges faced in tire aerodynamics with actual tire geometry, road contact and tire deformation. The article is an updated version of a recent book chapter [1]. The challenges include (1) the complexity of an actual tire geometry with longitudinal and transverse grooves, (2) the spin of the tire, (3) maintaining accurate representation of the boundary layers near the tire while being able to deal with the flow-domain topology change created by the road contact and tire deformation, and (4) the turbulent nature of the flow.

✉ Kenji Takizawa
Kenji.Takizawa@tafsm.org

Tayfun E. Tezduyar
tezduyar@tafsm.org

[1] Department of Modern Mechanical Engineering, Waseda University, 3-4-1 Ookubo, Shinjuku-ku, Tokyo 169-8555, Japan

[2] Mechanical Engineering, Rice University, MS 321, 6100 Main Street, Houston, TX 77005, USA

[3] Faculty of Science and Engineering, Waseda University, 3-4-1 Ookubo, Shinjuku-ku, Tokyo 169-8555, Japan

A new space–time (ST) computational method, "ST-SI-TC-IGA" [2], is enabling us to address the computational challenges. The ST-SI-TC-IGA was introduced [2] in the context of heart valve flow analysis. Its core component is the ST Variational Multiscale (ST-VMS) method [3–5], and the other key components are the ST Slip Interface (ST-SI) [6,7] and ST Topology Change (ST-TC) [8,9] methods and the ST Isogeometric Analysis (ST-IGA) [3,10,11].

1.1 ST-VMS

The ST-VMS is the VMS version of the Deforming-Spatial-Domain/Stabilized ST (DSD/SST) method [12–14]. The DSD/SST was introduced for computation of flows with moving boundaries and interfaces (MBI), including fluid–structure interactions (FSI). In MBI computations the DSD/SST functions as a moving-mesh method. Moving the fluid mechanics mesh to track an interface enables mesh-resolution control near the interface and, consequently, high-resolution boundary-layer representation near fluid–solid interfaces. The stabilization components of the DSD/SST are the Streamline-Upwind/Petrov-Galerkin (SUPG) [15] and Pressure-Stabilizing/Petrov-Galerkin (PSPG) [12] stabilizations, which are used very widely. Because of the SUPG and PSPG components, the DSD/SST is now also called "ST-SUPS." The VMS components of the ST-VMS are from the residual-based VMS (RBVMS) method [16–19]. There are two more stabilization terms beyond those in the ST-SUPS, and these additional terms give the method better turbulence modeling features. The ST-SUPS and ST-VMS, because of the higher-order accuracy of the ST framework (see [3,4]), are desirable also in computations without MBI.

The Arbitrary Lagrangian–Eulerian (ALE) method is an older and more commonly used moving-mesh method. The ALE-VMS method [20–25] is the VMS version of the ALE. It was introduced after the ST-SUPS [12] and ALE-SUPS [26] and preceded the ST-VMS. To increase their scope and accuracy, the ALE-VMS and RBVMS are often supplemented with special methods, such as those for weakly-enforced no-slip boundary conditions [27–29], "sliding interfaces" [30,31] and backflow stabilization [32]. They have been applied to many classes of FSI, MBI and fluid mechanics problems. The classes of problems include wind-turbine aerodynamics and FSI [33–40], more specifically, vertical-axis wind turbines [41,42], floating wind turbines [43], wind turbines in atmospheric boundary layers [44], and fatigue damage in wind-turbine blades [45], patient-specific cardiovascular fluid mechanics and FSI [20,46–51], biomedical-device FSI [52–57], ship hydrodynamics with free-surface flow and fluid–object interaction [58,59], hydrodynamics and FSI of a hydraulic arresting gear [60,61], hydrodynamics of tidal-stream turbines with free-surface flow [62], and bioinspired FSI for marine propulsion [63,64].

The ST-SUPS and ST-VMS have also been applied to many classes of FSI, MBI and fluid mechanics problems. The classes of problems include spacecraft parachute analysis for the landing-stage parachutes [23,65–68], cover-separation parachutes [69] and the drogue parachutes [70–72], wind-turbine aerodynamics for horizontal-axis wind-turbine rotors [23,33,73,74], full horizontal-axis wind-turbines [39,75–77] and vertical-axis wind-turbines [6,78], flapping-wing aerodynamics for an actual locust [10,23,79,80], bioinspired MAVs [76,77,81,82] and wing-clapping [8,83], blood flow analysis of cerebral aneurysms [76,84], stent-blocked aneurysms [84–86], aortas [87–90] and heart valves [2,8,9,77,89,91,92], spacecraft aerodynamics [69,93], thermo-fluid analysis of ground vehicles and their tires [5,91], thermo-fluid analysis of disk brakes [7], flow-driven string dynamics in turbomachinery [94,95], flow analysis of turbocharger turbines [11,96–98], flow around tires with road contact and deformation [1,91,99], ram-air parachutes [100], and compressible-flow spacecraft parachute aerodynamics [101,102].

In tire-aerodynamics computational analysis, the VMS feature of the ST-VMS addresses the challenge created by the turbulent nature of the flow, the moving-mesh feature of the ST framework enables high-resolution flow computation near the moving air–tire interface, and the higher-order accuracy of the ST framework strengthens both features. Furthermore, compared to the tire-aerodynamics computational analysis reported in [1], here we use newer element length definitions [103] for the stabilization parameters of the ST-VMS. The newer definitions are more suitable for isogeometric discretization.

1.2 ST-SI

The ST-SI was introduced in [6], in the context of incompressible-flow equations, to retain the desirable moving-mesh features of the ST-VMS and ST-SUPS when we have spinning solid surfaces, such as a turbine rotor. The mesh covering the spinning surface spins with it, retaining the high-resolution representation of the boundary layers. The starting point in the development of the ST-SI was the version of the ALE-VMS for computations with sliding interfaces [30,31]. Interface terms similar to those in the ALE-VMS version are added to the ST-VMS to account for the compatibility conditions for the velocity and stress at the SI. That accurately connects the two sides of the flow field. An ST-SI version where the SI is between fluid and solid domains with weakly-enforced Dirichlet boundary conditions for the fluid was also presented in [6]. The SI in this case is a "fluid–solid SI" rather than a standard "fluid–fluid SI." The ST-SI method introduced in [7] for the coupled incompressible-flow and thermal-transport equations retains the high-resolution representation of the thermo-fluid boundary layers near spinning

solid surfaces. These ST-SI methods have been applied to aerodynamic analysis of vertical-axis wind turbines [6,78], thermo-fluid analysis of disk brakes [7], flow-driven string dynamics in turbomachinery [94,95], flow analysis of turbocharger turbines [11,96–98], flow around tires with road contact and deformation [1,91,99], aerodynamic analysis of ram-air parachutes [100], and flow analysis of heart valves [2,89,92].

In another version of the ST-SI presented in [6], the SI is between a thin porous structure and the fluid on its two sides. This enables dealing with the fabric porosity in a fashion consistent with how the standard fluid–fluid SIs are dealt with and how the Dirichlet conditions are enforced weakly with fluid–solid SIs. Furthermore, this version enables handling thin structures that have T-junctions. This method has been applied to incompressible-flow aerodynamic analysis of ram-air parachutes with fabric porosity [100]. The compressible-flow ST-SI methods were introduced in [101], including the version where the SI is between a thin porous structure and the fluid on its two sides. Compressible-flow porosity models were also introduced in [101]. These, together with the compressible-flow ST SUPG method [104], extended the ST computational analysis range to compressible-flow aerodynamics of parachutes with fabric and geometric porosities. That enabled ST computational flow analysis of the Orion spacecraft drogue parachute in the compressible-flow regime [101,102].

In tire-aerodynamics computational analysis, the mesh covering the tire spins with it, and the SI between the spinning mesh and the rest of the mesh accurately connects the two sides of the solution. This enables high-resolution representation of the boundary layers near the tire. Furthermore, compared to the tire-aerodynamics computational analysis reported in [1], here we use newer element length definitions in [98] for the SI terms of the ST-SI. The newer definitions are more suitable for isogeometric discretization.

1.3 ST-TC

The ST-TC [8,9] was introduced for moving-mesh computation of flow problems with TC, such as contact between solid surfaces. Even before the ST-TC, the ST-SUPS and ST-VMS, when used with robust mesh update methods, have proven effective in flow computations where the solid surfaces are in near contact or create other near TC, if the nearness is sufficiently near for the purpose of solving the problem. Many classes of problems can be solved that way with sufficient accuracy. For examples of such computations, see the references mentioned in [8]. The ST-TC made moving-mesh computations possible even when there is an actual contact between solid surfaces or other TC. By collapsing elements as needed, without changing the connectivity of the "parent" mesh, the ST-TC can handle an actual TC while maintaining high-resolution boundary layer representation near solid surfaces. This enabled successful moving-mesh computation of heart valve flows [2,8,9,77,89,91,92], wing clapping [83], and flow around a rotating tire with road contact and prescribed deformation [1,91,99].

In tire-aerodynamics computational analysis, the ST-TC enables moving-mesh computation even with the TC created by the actual contact between the tire and the road. It deals with the contact while maintaining high-resolution flow representation near the tire.

1.4 ST-SI-TC

The ST-SI-TC is the integration of the ST-SI and ST-TC. A fluid–fluid SI requires elements on both sides of the SI. When part of an SI needs to coincide with a solid surface, which happens for example when the solid surfaces on two sides of an SI come into contact or when an SI reaches a solid surface, the elements between the coinciding SI part and the solid surface need to collapse with the ST-TC mechanism. The collapse switches the SI from fluid–fluid SI to fluid–solid SI. With that, an SI can be a mixture of fluid–fluid and fluid–solid SIs. With the ST-SI-TC, the elements collapse and are reborn independent of the nodes representing a solid surface. The ST-SI-TC enables high-resolution flow representation even when parts of the SI are coinciding with a solid surface. It also enables dealing with contact location change and contact sliding. This was applied to heart valve flow analysis [2,89,92] and tire aerodynamics with road contact and deformation [1,99].

In tire-aerodynamics computational analysis, the ST-SI-TC enables high-resolution flow representation even though parts of the SI are coinciding with the tire and road surfaces. It also enables dealing with tire–road contact location change and contact sliding. Furthermore, compared to the tire-aerodynamics computational analysis reported in [1], the newer element length definitions [98] used here for the SI terms of the ST-SI are more robust in the SI-TC mechanism, even with finite element discretization.

1.5 ST-IGA

The ST-IGA was introduced in [3]. It is the integration of the ST framework with isogeometric discretization. First computations with the ST-VMS and ST-IGA were reported in [3] in a 2D context, with IGA basis functions in space for flow past an airfoil, and in both space and time for the advection equation. The stability and accuracy analysis given [3] for the advection equation showed that using higher-order basis functions in time would be essential in getting full benefit out of using higher-order basis functions in space.

In the early stages of the ST-IGA, the emphasis was on IGA basis functions in time. As pointed out in [3,4] and

demonstrated in [10,79,81], higher-order NURBS basis functions in time provide a more accurate representation of the motion of the solid surfaces and a mesh motion consistent with that. They also provide more efficiency in temporal representation of the motion and deformation of the volume meshes, and better efficiency in remeshing. That motivated the development of the ST/NURBS Mesh Update Method (STNMUM) [10,79,81]. The name "STNMUM" was given in [75]. The STNMUM has a wide scope that includes spinning solid surfaces. With the spinning motion represented by quadratic NURBS basis functions in time, and with sufficient number of temporal patches for a full rotation, the circular paths are represented exactly, and a "secondary mapping" [3,4,10,23] enables also specifying a constant angular velocity for invariant speeds along the paths. The ST framework and NURBS in time also enable, with the "ST-C" method, extracting a continuous representation from the computed data and, in large-scale computations, efficient data compression [5,7,91,94,95,105]. The STNMUM and desirable features of the ST-IGA with IGA basis functions in time have been demonstrated in many 3D computations. The classes of problems solved are flapping-wing aerodynamics for an actual locust [10,23,79,80], bioinspired MAVs [76,77,81,82] and wing-clapping [8,83], separation aerodynamics of spacecraft [69], aerodynamics of horizontal-axis [39,75–77] and vertical-axis [6,78] wind-turbines, thermo-fluid analysis of ground vehicles and their tires [5,91], thermo-fluid analysis of disk brakes [7], flow-driven string dynamics in turbomachinery [94,95], and flow analysis of turbocharger turbines [11,96–98].

The ST-IGA with IGA basis functions in space have been utilized in ST computational flow analysis of turbocharger turbines [11,96–98], flow-driven string dynamics in turbomachinery [95], ram-air parachutes [100], spacecraft parachutes [102], aortas [89,90], heart valves [2,89,92], and tires with road contact and deformation [1]. Most of these computations were accomplished with the integration of the ST-IGA and ST-SI or ST-IGA, ST-SI and ST-TC.

1.6 ST-SI-TC-IGA

The turbocharger turbine analysis [11,96–98] and flow-driven string dynamics in turbomachinery [95] were based on the integration of the ST-SI and ST-IGA. The IGA basis functions were used in the spatial discretization of the fluid mechanics equations and also in the temporal representation of the rotor and spinning-mesh motion. That enabled accurate representation of the turbine geometry and rotor motion and increased accuracy in the flow solution. The IGA basis functions were used also in the spatial discretization of the string structural dynamics equations. This enabled increased accuracy in the structural dynamics solution, as well as smoothness in the string shape and fluid dynamics forces computed on the string.

The ram-air parachute analysis [100] and spacecraft parachute compressible-flow analysis [102] were based on the integration of the ST-IGA, the ST-SI version that weakly enforces the Dirichlet conditions, and the ST-SI version that accounts for the porosity of a thin structure. The ST-IGA with IGA basis functions in space enabled, with relatively few number of unknowns, accurate representation of the parafoil and parachute geometries and increased accuracy in the flow solution. The volume mesh needed to be generated both inside and outside the parafoil. Mesh generation inside was challenging near the trailing edge because of the narrowing space. The spacecraft parachute has a very complex geometry, including gores and gaps. Using IGA basis functions addressed those challenges and still kept the element density near the trailing edge of the parafoil and around the spacecraft parachute at a reasonable level.

The heart valve analysis [2,89,92] was based on the integration of the ST-SI, ST-TC and ST-IGA. The ST-SI-TC-IGA, beyond enabling a more accurate representation of the geometry and increased accuracy in the flow solution, kept the element density in the narrow spaces near the contact areas at a reasonable level. When solid surfaces come into contact, the elements between the surface and the SI collapse. Before the elements collapse, the boundaries could be curved and rather complex, and the narrow spaces might have high-aspect-ratio elements. With NURBS elements, it was possible to deal with such adverse conditions rather effectively.

An SI provides mesh generation flexibility in a general context by accurately connecting the two sides of the solution computed over nonmatching meshes. This type of mesh generation flexibility is especially valuable in complex-geometry flow computations with isogeometric discretization, removing the matching requirement between the NURBS patches without loss of accuracy. This feature was used in the flow analysis of heart valves [2,89,92], turbocharger turbines [11,96–98], and spacecraft parachute compressible-flow analysis [102].

In tire-aerodynamics computational analysis, the ST-SI-TC-IGA enables a more accurate representation of the geometry and motion of the tire surfaces, a mesh motion consistent with that, and increased accuracy in the flow solution. It also keeps the element density in the tire grooves and in the narrow spaces near the contact areas at a reasonable level. In addition, we benefit from the mesh generation flexibility provided by using SIs.

1.7 Tire models

We present computations with the ST-SI-TC-IGA and two models of flow around a rotating tire with road contact and

prescribed deformation. One is a simple 2D model for verification purposes, and one is a 3D model with an actual tire geometry and a deformation pattern provided by the tire company.

1.8 Outline of the remaining sections

In Sect. 2 we describe the ST-VMS and ST-SI. The ST-SI-TC-IGA is described in Sect. 3. The computations with the 2D and 3D models are presented in Sects. 4 and 5, and the concluding remarks are given in Sect. 6.

2 ST-VMS and ST-SI

For completeness, we include, mostly from [6,99], the ST-VMS and ST-SI methods.

2.1 ST-VMS

The ST-VMS is given as

$$\begin{aligned}
&\int_{Q_n} \mathbf{w}^h \cdot \rho \left(\frac{\partial \mathbf{u}^h}{\partial t} + \mathbf{u}^h \cdot \nabla \mathbf{u}^h - \mathbf{f}^h \right) \mathrm{d}Q \\
&\quad + \int_{Q_n} \boldsymbol{\varepsilon}(\mathbf{w}^h) : \boldsymbol{\sigma}(\mathbf{u}^h, p^h) \mathrm{d}Q - \int_{(P_n)_\mathrm{h}} \mathbf{w}^h \cdot \mathbf{h}^h \mathrm{d}P \\
&\quad + \int_{Q_n} q^h \nabla \cdot \mathbf{u}^h \mathrm{d}Q + \int_{\Omega_n} (\mathbf{w}^h)_n^+ \cdot \rho \left((\mathbf{u}^h)_n^+ - (\mathbf{u}^h)_n^- \right) \mathrm{d}\Omega \\
&\quad + \sum_{e=1}^{(n_\mathrm{el})_n} \int_{Q_n^e} \frac{\tau_\mathrm{SUPS}}{\rho} \left[\rho \left(\frac{\partial \mathbf{w}^h}{\partial t} + \mathbf{u}^h \cdot \nabla \mathbf{w}^h \right) \right. \\
&\qquad \left. + \nabla q^h \right] \cdot \mathbf{r}_\mathrm{M}(\mathbf{u}^h, p^h) \mathrm{d}Q \\
&\quad + \sum_{e=1}^{(n_\mathrm{el})_n} \int_{Q_n^e} \nu_\mathrm{LSIC} \nabla \cdot \mathbf{w}^h \rho r_\mathrm{C}(\mathbf{u}^h) \mathrm{d}Q \\
&\quad - \sum_{e=1}^{(n_\mathrm{el})_n} \int_{Q_n^e} \tau_\mathrm{SUPS} \mathbf{w}^h \cdot \left(\mathbf{r}_\mathrm{M}(\mathbf{u}^h, p^h) \cdot \nabla \mathbf{u}^h \right) \mathrm{d}Q \\
&\quad - \sum_{e=1}^{(n_\mathrm{el})_n} \int_{Q_n^e} \frac{\tau_\mathrm{SUPS}^2}{\rho} \mathbf{r}_\mathrm{M}(\mathbf{u}^h, p^h) \cdot \left(\nabla \mathbf{w}^h \right) \cdot \mathbf{r}_\mathrm{M}(\mathbf{u}^h, p^h) \mathrm{d}Q \\
&= 0, \qquad (1)
\end{aligned}$$

where

$$\mathbf{r}_\mathrm{M}(\mathbf{u}^h, p^h) = \rho \left(\frac{\partial \mathbf{u}^h}{\partial t} + \mathbf{u}^h \cdot \nabla \mathbf{u}^h - \mathbf{f}^h \right) - \nabla \cdot \boldsymbol{\sigma}(\mathbf{u}^h, p^h), \qquad (2)$$

$$r_\mathrm{C}(\mathbf{u}^h) = \nabla \cdot \mathbf{u}^h \qquad (3)$$

are the residuals of the momentum equation and incompressibility constraint. Here, ρ, $\mathbf{u}$, p, $\mathbf{f}$, and $\mathbf{h}$ are the density, velocity, pressure, body force, and the stress specified at the boundary. The stress tensor is defined as $\boldsymbol{\sigma}(\mathbf{u}, p) = -p\mathbf{I} + 2\mu\boldsymbol{\varepsilon}(\mathbf{u})$, where $\mathbf{I}$ is the identity tensor, $\mu = \rho\nu$ is the viscosity, ν is the kinematic viscosity, and $\boldsymbol{\varepsilon}(\mathbf{u}) = \left((\nabla \mathbf{u}) + (\nabla \mathbf{u})^T \right)/2$ is the strain-rate tensor. The test functions associated with the $\mathbf{u}$ and p are $\mathbf{w}$ and q. A superscript "h" indicates that the function is coming from a finite-dimensional space. The symbol Q_n represents the ST slice between time levels n and $n+1$, $(P_n)_\mathrm{h}$ is the part of the slice lateral boundary associated with the boundary condition $\mathbf{h}$, and Ω_n is the spatial domain at time level n. The superscript "e" is the ST element counter, and n_el is the number of ST elements. The functions are discontinuous in time at each time level, and the superscripts "$-$" and "$+$" indicate the values of the functions just below and above the time level.

Remark 1 The ST-SUPS can be obtained from the ST-VMS by dropping the eighth and ninth integrations.

The way the stabilization parameters τ_SUPS and ν_LSIC are calculated has been evolving since the inception of the SUPG method. Here, τ_SUPS is mostly from [103]:

$$\tau_\mathrm{SUPS} = \left(\tau_\mathrm{SUGN12}^{-2} + \tau_\mathrm{SUGN3}^{-2} + \tau_\mathrm{SUGN4}^{-2} \right)^{-\frac{1}{2}}. \qquad (4)$$

The first component is given as

$$\tau_\mathrm{SUGN12}^{-2} = \begin{bmatrix} 1 \\ \mathbf{u} \end{bmatrix} \begin{bmatrix} 1 \\ \mathbf{u} \end{bmatrix} : \mathbf{G}^\mathrm{ST}, \qquad (5)$$

where $\mathbf{G}^\mathrm{ST}$ is the element metric tensor in the ST framework (see Appendix 2). The second component is defined as

$$\tau_\mathrm{SUGN3}^{-1} = \nu \mathbf{r}\mathbf{r} : \mathbf{G}, \qquad (6)$$

where $\mathbf{r}$ is the solution direction:

$$\mathbf{r} = \frac{\nabla \|\mathbf{u}\|}{\|\nabla \|\mathbf{u}\|\|}, \qquad (7)$$

and $\mathbf{G}$ is the element metric tensor (see Appendix 1). The third component, originating from [5], is defined as

$$\tau_\mathrm{SUGN4} = \left\| \nabla \mathbf{u}^h \right\|_F^{-1}, \qquad (8)$$

where $\|\cdot\|_F$ is the Frobenius norm. The stabilization parameter ν_LSIC is from [75]:

$$\nu_\mathrm{LSIC} = \frac{h_\mathrm{LSIC}^2}{\tau_\mathrm{SUPS}}, \qquad (9)$$

with h_LSIC set equal to the minimum element length h_MIN (see Appendix 1). For more ways of calculating the stabilization parameters, see [5,6,13,14,75,106–127].

2.2 ST-SI

2.2.1 Two-side formulation (fluid–fluid SI)

In describing the ST-SI, labels "Side A" and "Side B" will represent the two sides of the SI. The ST-SI version of the formulation given by Eq. (1) includes added boundary terms corresponding to the SI. The boundary terms for the two sides are first added separately, using test functions $\mathbf{w}_{\mathrm{A}}^h$ and q_{A}^h and $\mathbf{w}_{\mathrm{B}}^h$ and q_{B}^h. Then, putting together the terms added to each side, the complete set of terms added becomes

$$
\begin{aligned}
&-\int_{(P_n)_{\mathrm{SI}}} \left(q_{\mathrm{B}}^h \mathbf{n}_{\mathrm{B}} - q_{\mathrm{A}}^h \mathbf{n}_{\mathrm{A}}\right) \cdot \frac{1}{2}\left(\mathbf{u}_{\mathrm{B}}^h - \mathbf{u}_{\mathrm{A}}^h\right) \mathrm{d}P \\
&\quad -\int_{(P_n)_{\mathrm{SI}}} \rho \mathbf{w}_{\mathrm{B}}^h \cdot \frac{1}{2}\left(\left(\mathcal{F}_{\mathrm{B}}^h - \left|\mathcal{F}_{\mathrm{B}}^h\right|\right)\mathbf{u}_{\mathrm{B}}^h \right. \\
&\qquad\qquad \left. -\left(\mathcal{F}_{\mathrm{B}}^h - \left|\mathcal{F}_{\mathrm{B}}^h\right|\right)\mathbf{u}_{\mathrm{A}}^h\right) \mathrm{d}P \\
&\quad -\int_{(P_n)_{\mathrm{SI}}} \rho \mathbf{w}_{\mathrm{A}}^h \cdot \frac{1}{2}\left(\left(\mathcal{F}_{\mathrm{A}}^h - \left|\mathcal{F}_{\mathrm{A}}^h\right|\right)\mathbf{u}_{\mathrm{A}}^h \right. \\
&\qquad\qquad \left. -\left(\mathcal{F}_{\mathrm{A}}^h - \left|\mathcal{F}_{\mathrm{A}}^h\right|\right)\mathbf{u}_{\mathrm{B}}^h\right) \mathrm{d}P \\
&\quad +\int_{(P_n)_{\mathrm{SI}}} \left(\mathbf{n}_{\mathrm{B}} \cdot \mathbf{w}_{\mathrm{B}}^h + \mathbf{n}_{\mathrm{A}} \cdot \mathbf{w}_{\mathrm{A}}^h\right) \frac{1}{2}\left(p_{\mathrm{B}}^h + p_{\mathrm{A}}^h\right) \mathrm{d}P \\
&\quad -\int_{(P_n)_{\mathrm{SI}}} \left(\mathbf{w}_{\mathrm{B}}^h - \mathbf{w}_{\mathrm{A}}^h\right) \cdot \left(\hat{\mathbf{n}}_{\mathrm{B}} \cdot \mu\left(\boldsymbol{\varepsilon}(\mathbf{u}_{\mathrm{B}}^h) + \boldsymbol{\varepsilon}(\mathbf{u}_{\mathrm{A}}^h)\right)\right) \mathrm{d}P \\
&\quad -\gamma \int_{(P_n)_{\mathrm{SI}}} \hat{\mathbf{n}}_{\mathrm{B}} \cdot \mu\left(\boldsymbol{\varepsilon}\left(\mathbf{w}_{\mathrm{B}}^h\right) + \boldsymbol{\varepsilon}\left(\mathbf{w}_{\mathrm{A}}^h\right)\right) \cdot \left(\mathbf{u}_{\mathrm{B}}^h - \mathbf{u}_{\mathrm{A}}^h\right) \mathrm{d}P \\
&\quad +\int_{(P_n)_{\mathrm{SI}}} \frac{\mu C}{h}\left(\mathbf{w}_{\mathrm{B}}^h - \mathbf{w}_{\mathrm{A}}^h\right) \cdot \left(\mathbf{u}_{\mathrm{B}}^h - \mathbf{u}_{\mathrm{A}}^h\right) \mathrm{d}P, \qquad (10)
\end{aligned}
$$

where

$$\mathcal{F}_{\mathrm{B}}^h = \mathbf{n}_{\mathrm{B}} \cdot \left(\mathbf{u}_{\mathrm{B}}^h - \mathbf{v}_{\mathrm{B}}^h\right), \qquad (11)$$

$$\mathcal{F}_{\mathrm{A}}^h = \mathbf{n}_{\mathrm{A}} \cdot \left(\mathbf{u}_{\mathrm{A}}^h - \mathbf{v}_{\mathrm{A}}^h\right), \qquad (12)$$

$$h = \left(\frac{h_{\mathrm{B}}^{-1} + h_{\mathrm{A}}^{-1}}{2}\right)^{-1}, \qquad (13)$$

$$h_{\mathrm{B}} = 2\left(\mathbf{n}_{\mathrm{B}}\mathbf{n}_{\mathrm{B}} : \mathbf{G}\right)^{-\frac{1}{2}} \quad \text{(for Side B)}, \qquad (14)$$

$$h_{\mathrm{A}} = 2\left(\mathbf{n}_{\mathrm{A}}\mathbf{n}_{\mathrm{A}} : \mathbf{G}\right)^{-\frac{1}{2}} \quad \text{(for Side A)}, \qquad (15)$$

$$\hat{\mathbf{n}}_{\mathrm{B}} = \frac{\mathbf{n}_{\mathrm{B}} - \mathbf{n}_{\mathrm{A}}}{\|\mathbf{n}_{\mathrm{B}} - \mathbf{n}_{\mathrm{A}}\|}. \qquad (16)$$

Here, $(P_n)_{\mathrm{SI}}$ is the SI in the ST domain, $\mathbf{n}$ is the unit normal vector, $\mathbf{v}$ is the mesh velocity, $\gamma = 1$, and C is a nondimensional constant. We note that the expressions given by Eqs. (13)–(15) were introduced in published form in [98]. At the same time we note that the element lengths given by Eqs. (14) and (15) are straightforward extensions of the one in [103]. For explanation of the added SI terms, see [6].

2.2.2 One-side formulation (fluid–solid SI)

On solid surfaces where we prefer weak enforcement of the Dirichlet conditions [27,29] for the fluid, we use the ST-SI version where the SI is between the fluid and solid domains. This version is obtained (see [6]) by starting with the terms added to Side B and replacing the Side A velocity with the velocity $\mathbf{g}^h$ coming from the solid domain. Then the SI terms added to Eq. (1) to represent the weakly-enforced Dirichlet conditions become

$$
\begin{aligned}
&-\int_{(P_n)_{\mathrm{SI}}} q_{\mathrm{B}}^h \mathbf{n}_{\mathrm{B}} \cdot \mathbf{u}_{\mathrm{B}}^h \mathrm{d}P - \int_{(P_n)_{\mathrm{SI}}} \rho \mathbf{w}_{\mathrm{B}}^h \cdot \mathcal{F}_{\mathrm{B}}^h \mathbf{u}_{\mathrm{B}}^h \mathrm{d}P \\
&\quad +\int_{(P_n)_{\mathrm{SI}}} q_{\mathrm{B}}^h \mathbf{n}_{\mathrm{B}} \cdot \mathbf{g}^h \mathrm{d}P \\
&\quad +\int_{(P_n)_{\mathrm{SI}}} \rho \mathbf{w}_{\mathrm{B}}^h \cdot \frac{1}{2}\left(\left(\mathcal{F}_{\mathrm{B}}^h + \left|\mathcal{F}_{\mathrm{B}}^h\right|\right)\mathbf{u}_{\mathrm{B}}^h \right. \\
&\qquad\qquad \left. +\left(\mathcal{F}_{\mathrm{B}}^h - \left|\mathcal{F}_{\mathrm{B}}^h\right|\right)\mathbf{g}^h\right) \mathrm{d}P \\
&\quad -\int_{(P_n)_{\mathrm{SI}}} \mathbf{w}_{\mathrm{B}}^h \cdot \left(\mathbf{n}_{\mathrm{B}} \cdot \boldsymbol{\sigma}_{\mathrm{B}}^h\right) \mathrm{d}P \\
&\quad -\gamma \int_{(P_n)_{\mathrm{SI}}} \mathbf{n}_{\mathrm{B}} \cdot 2\mu\boldsymbol{\varepsilon}\left(\mathbf{w}_{\mathrm{B}}^h\right) \cdot \left(\mathbf{u}_{\mathrm{B}}^h - \mathbf{g}^h\right) \mathrm{d}P \\
&\quad +\int_{(P_n)_{\mathrm{SI}}} \frac{\mu C}{h_{\mathrm{B}}} \mathbf{w}_{\mathrm{B}}^h \cdot \left(\mathbf{u}_{\mathrm{B}}^h - \mathbf{g}^h\right) \mathrm{d}P. \qquad (17)
\end{aligned}
$$

3 ST-SI-TC-IGA

For completeness, we include (1) from [2,99] the aspects of the ST-SI [6] and ST-TC [8] related to their integration as the ST-SI-TC [99] and the advantages of the IGA in this context, and (2) from [2] the integration of all three components as the ST-SI-TC-IGA.

3.1 ST-SI

The ST-SI allows mesh slipping also in the one-side formulation, that is, when the SI serves the purpose of weak enforcement of the Dirichlet boundary conditions for the fluid. The boundary terms added to Eq. (1) to connect the two sides in the fluid–fluid SI and to connect the fluid to the solid in the fluid–solid SI were given in Sects. 2.2.1 and 2.2.2. The added terms [see Eqs. (10) and (17)] include derivatives in the direction normal to the SI. Therefore the elements bordering the SI need to have finite thickness in the normal direction. This places a limitation on the meshes that can be used with the ST-SI; elements bordering the SI cannot have zero thickness in the normal direction when they degenerate.

3.2 ST-TC

The ST-TC can deal with TC in ST moving-mesh computations. The discretization is unstructured in time, but based on a parent ST mesh that is structured in time, and the parent mesh is extruded from a single spatial mesh. The key technology in the ST-TC is massive element degeneration by using a special master–slave system. The special system allows changing, in an ST slab, master nodes to slave nodes and slave nodes to master nodes. With that, elements can collapse or be reborn. This way, in an ST slab, we can represent closing and opening motions. Since an ST method naturally allows discretizations that are unstructured in time, no further modification is needed. With the ST-TC, we have a method that is very flexible, and computationally as effective as a typical moving-mesh method. However, the master–slave relationship has to be node to node; a point on a solid surface that is not a node cannot be a master or slave node.

3.3 ST-IGA

With NURBS meshes, we can represent curved boundaries with less elements compared to finite element meshes. With this desirable feature, a volume can be meshed also with high-aspect-ratio elements. This is particularly helpful when we need to generate meshes in very narrow spaces.

3.4 ST-SI-TC-IGA

Integration of the ST-SI, ST-TC and ST-IGA brings several good features to ST computations. (1) It enables high-resolution boundary layer representation near the solid surfaces in contact even when the surfaces are covered by meshes with SI. (2) It enables dealing with contact location change and contact sliding on the SI. This overcomes the ST-TC restriction created by the rule that a point on a solid surface that is not a node cannot be a master or slave node. (3) When part of an SI needs to coincide with a solid surface, which happens for example when the solid surfaces on two sides of an SI come into contact or when an SI reaches a solid surface, the elements between the coinciding SI part and the solid surface need to collapse with the ST-TC mechanism. Before the elements collapse, the boundaries could be curved and complex, and the narrow space might have high-aspect-ratio elements. With NURBS elements, we can deal with such adverse conditions rather effectively.

Figure 1 is an example of Case (1), where we have a spinning solid surface in contact with a planar solid surface. An SI is created around the spinning surface (see Fig. 2).

The SI allows the solid surface spin together with the mesh around it. The elements collapsed with the ST-TC mechanism are in the stationary mesh on the lower side of the SI and in the spinning mesh in the contact area. The collapse decision,

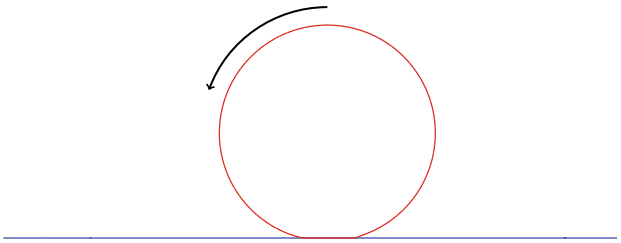

Fig. 1 A spinning solid surface (red) in contact with a planar solid surface (blue), with no slip between the surfaces. (Color figure online)

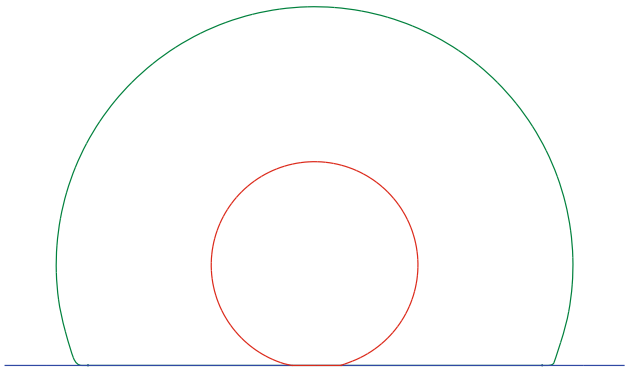

Fig. 2 A spinning solid surface (red) in contact with a planar solid surface (blue). The green line is the SI. It coincides with the blue line and the flat part of the red line. (Color figure online)

which is the selection between the two-side and one-side formulations, is made integration-point-wise, for each side separately, based on the element length in the normal direction, as given by Eqs. (14) and (15). For example, for Side B, the decision at an integration point is made with the following rules:

- If $h_{\mathrm{B}} = 0$, we disregard the integration point, regardless of the value of h_{A}.
- If $h_{\mathrm{B}} > 0$ and $h_{\mathrm{A}} = 0$, we use the one-side formulation.
- In other cases, we use the two-side formulation.

Figures 3 and 4 illustrate how the ST-SI-TC-IGA works.

We note that the SI has a high curvature where it meets the planar surface. To improve the geometric match between the two sides of the SI there, we limit the motion of one of the control points. This in turn reduces the motion of the control points nearby. We periodically remove that limitation for a very short duration, resulting in a sudden jump in the positions of those control points, as can bee seen in the 4th and 5th frames of Figs. 3 and 4.

Remark 2 A node on an SI coinciding with a solid surface must be a slave of the corresponding node on that solid surface.

Remark 3 When for all integration points of an element surface (element edge in the context of the 2D examples) h_{B}

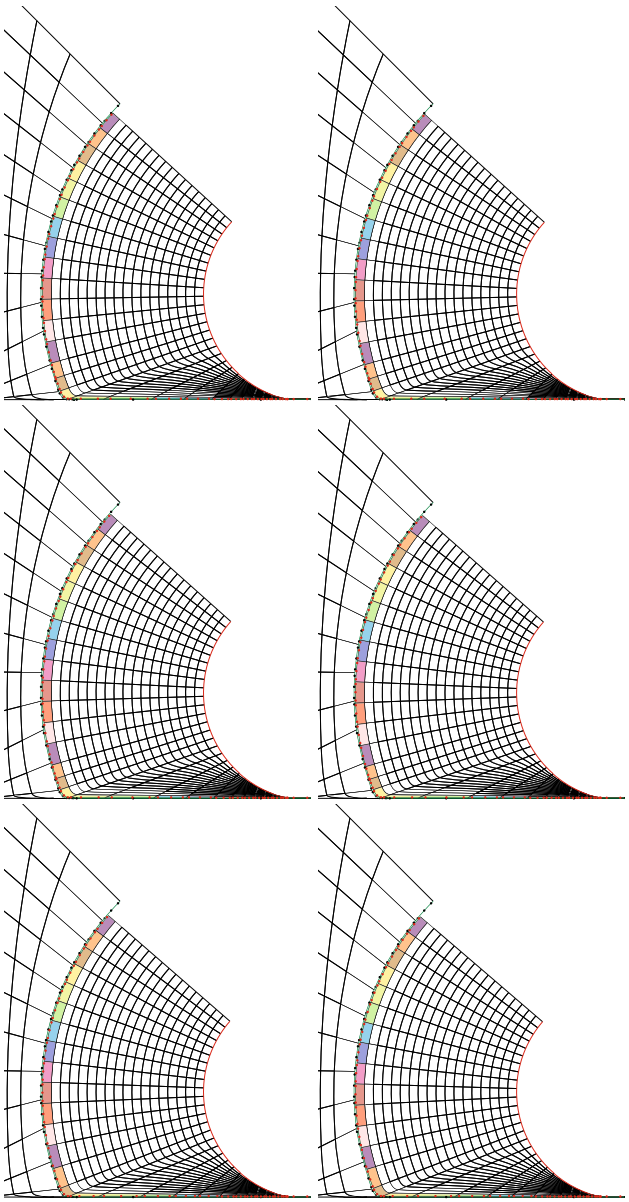

Fig. 3 Illustration of how the ST-SI-TC-IGA works for the example in Figs. 1 and 2. A part of the control mesh is shown. The red and black points (more visible when zooming around the SI) are the integration points on the two sides of the SI. The outer part of the mesh is on the stationary side of the SI, and the inner part is rotating with the spinning surface (red). The elements collapsed with the ST-TC mechanism are in the stationary mesh on the lower side of the green surface and in the spinning mesh in the contact area. The element coloring on the inner side of the SI is for better visualization of the mesh motion. (Color figure online)

$= h_A = 0$, that surface is a contact surface. Pressure is not treated as an unknown at a solid-surface master node whose all slave SI nodes live only on contact surfaces. That node has no role in the equation system beyond representing the geometry. Consequently, mesh resolution plays no role in regions made of only contact surfaces. For that reason, in

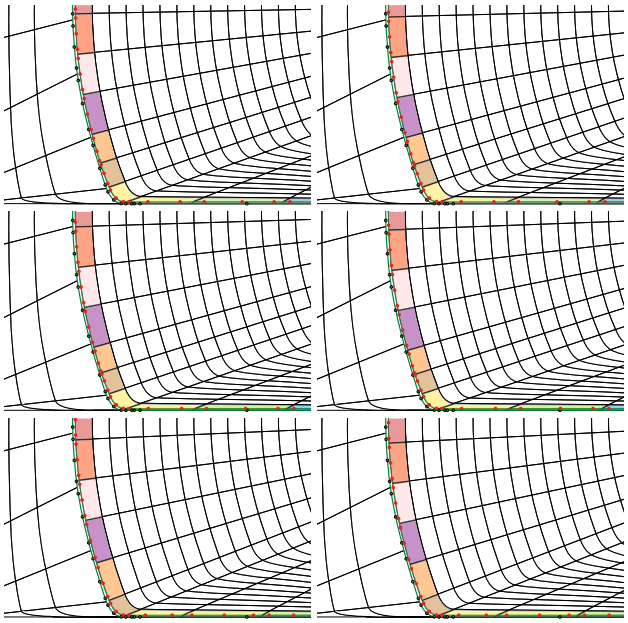

Fig. 4 The close-up view of Fig. 3, where the collapsed elements are only on the stationary side of the SI. The method switches to the one-side formulation on the part of the SI coinciding with the planar surface, and remains as the two-side formulation on the other parts

Fig. 4, the stationary mesh in the contact area has very few elements.

4 Verification with a simple 2D model

In this problem a nonmoving mesh can be used to obtain the solution. That will be the reference solution we will compare the ST-SI-TC-IGA solution to for verification purposes. We will also conduct a verification study by comparing the solutions from two meshes with different refinements.

4.1 Problem setup

A spinning solid surface is in contact with a planar solid surface and undergoes deformation. The geometry of the model and the deformation pattern are shown in Fig. 5. The rotation speed corresponds to a linear speed of $U = 100$ km/h at the undeformed tire periphery. There is no slip between the spinning and planar surfaces. The speed of the planar surface becomes

$$U_0 = \frac{\sin\theta}{\theta} U, \tag{18}$$

where $\theta = 15°$, giving $U_0 = 98.86$ km/h. The density and kinematic viscosity of the air are $1.205\,\mathrm{kg/m^3}$ and $1.512 \times 10^{-5}\,\mathrm{m^2/s}$.

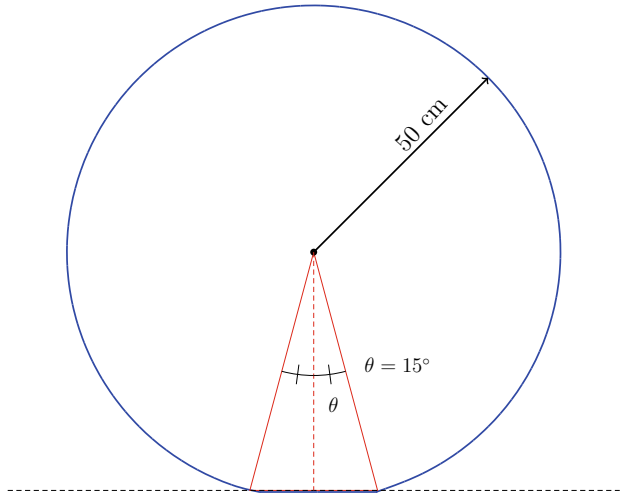

Fig. 5 A simple 2D model. The deformation region is the circular sector with central angle 30°

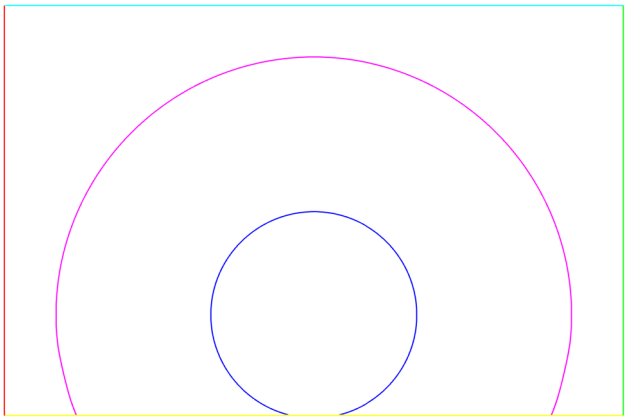

Fig. 6 A simple 2D model. Computational domain and boundary conditions. The left (red) and bottom (yellow) boundaries represent the inflow and the moving planar surface, where the velocity is U_0. The innermost (blue) circle is the spinning surface, where the velocity is U. The larger (pink) circle is the SI. The bottom of the SI is coinciding with the planar surface and the interface of the spinning and planar surfaces. The conditions at the right (green) and upper (cyan) boundaries are stress-free and slip, respectively. (Color figure online)

4.2 Computational domain, boundary conditions and meshes

Figure 6 shows the computational domain and boundary conditions. The domain size is 3.00 m × 1.98 m. We use two different quadratic NURBS meshes: a preliminary mesh and a refined mesh. Near the tire surface, the refined mesh has twice the resolution in both the circumferential and normal directions. Figure 7 shows the preliminary mesh. The number of control points and elements are 2204 and 1800. We note that the higher normal-direction mesh resolution on the inner side of the SI is for better boundary-layer resolution where the SI coincides with the road surface. The SI is not needed for nonmoving-mesh computations, but we include it in computing the reference solution so that the mesh for the reference solution is just the "frozen" version of the mesh for the ST-SI-TC-IGA solution. Figure 8 shows the moving mesh at different instants during the computation with the ST-SI-TC-IGA. Figure 9 shows the mesh near the contact area during the period between the 6th and 7th frames in Fig. 8. Figure 10 shows the refined mesh. The number of control points and elements are 7992 and 7200.

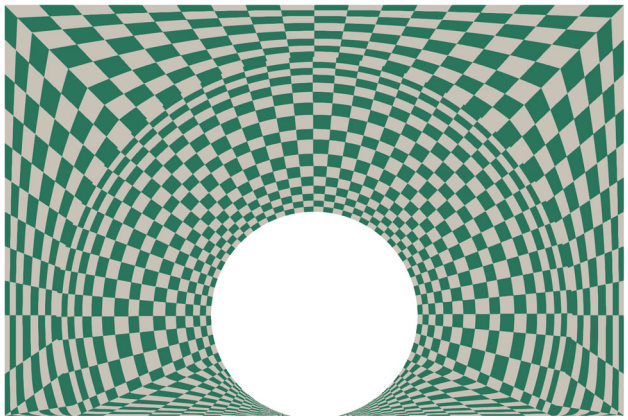

Fig. 7 A simple 2D model. Preliminary mesh. The number of control points and elements are 2204 and 1800. The checkerboard coloring is for differentiating between the NURBS elements

4.3 Computational conditions

In the computations with the preliminary mesh, there are 1000 time steps per rotation, which is equivalent to a time-step size of 1.131×10^{-4} s. In the refined-mesh computations, the time-step size is reduced to half of the value used with the preliminary mesh, making it 5.655×10^{-5} s. The number of nonlinear iterations per time step is 3, and the number of GMRES [128] iterations per nonlinear iteration is 300.

4.4 Results

Figures 11 and 12 show the velocity magnitude from the preliminary-mesh computations with the nonmoving-mesh (ST-SI-IGA) and ST-SI-TC-IGA methods. Overall, the results from the two computations are very comparable.

Figure 13 shows the horizontal component of the flow velocity computed with the nonmoving-mesh (ST-SI-IGA) method, using the preliminary and refined meshes. The spinning surface generates a flow relative to the planar surface, creating boundary layers near the spinning and planar surfaces. The preliminary-mesh solution has just slightly more fluctuations than the refined-mesh solution, and we can see convergence.

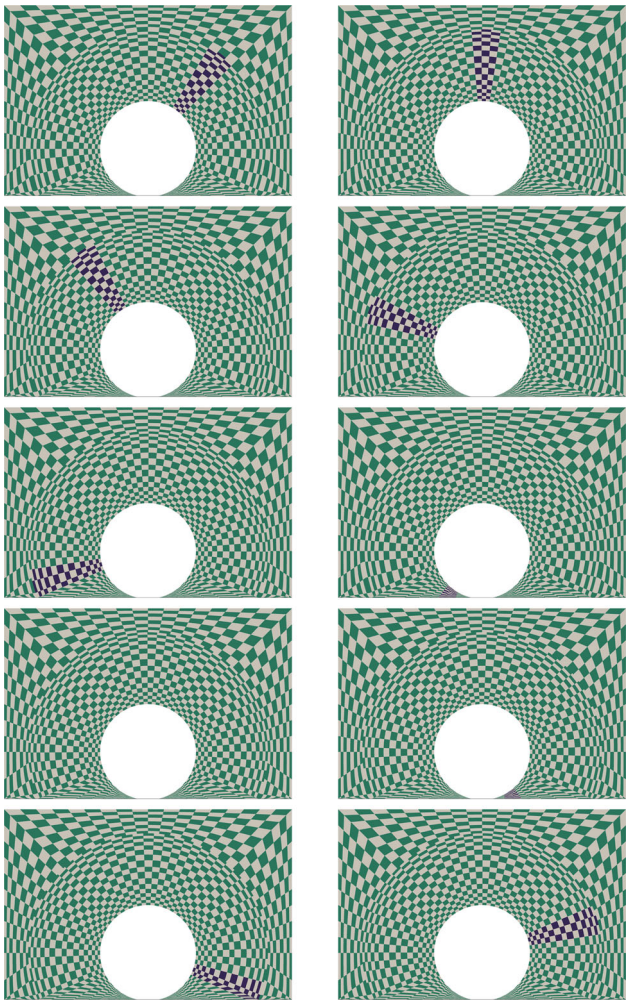

Fig. 8 A simple 2D model. Preliminary mesh at uniformly spaced instants during a one-rotation computation with the ST-SI-TC-IGA. The checkerboard coloring is for differentiating between the NURBS elements. A band of elements in the inner mesh are colored blue to illustrate the mesh rotation. (Color figure online)

To compare the solutions obtained with the ST-SI-TC-IGA and nonmoving-mesh (ST-SI-IGA) methods, Figs. 14 and 15 show the horizontal component of the flow velocity computed with these two methods, using the preliminary and refined meshes. The solutions obtained with the two methods are in close agreement, indicating that the ST-SI-TC-IGA method can accurately represent the boundary layers in this class of flow problems, including the boundary layers in regions near the contact.

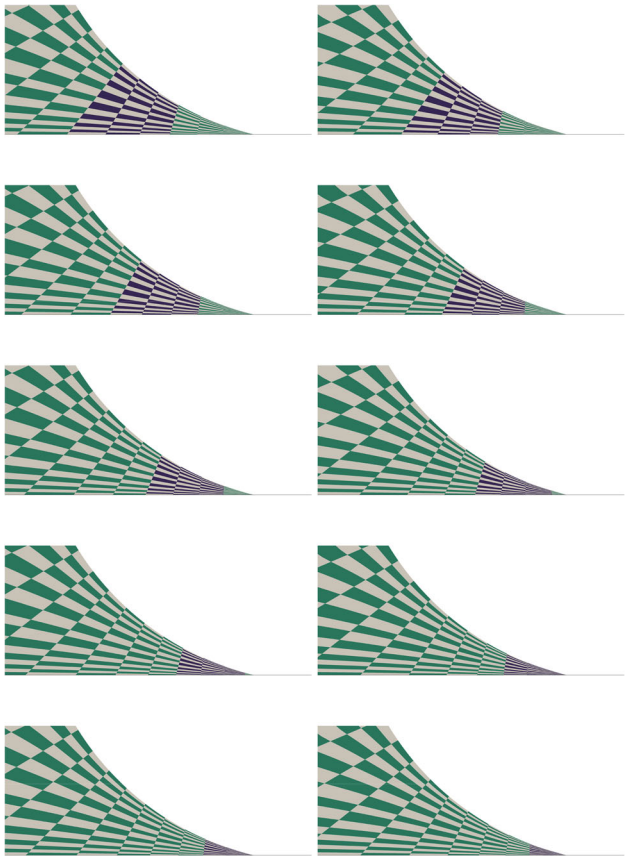

Fig. 9 A simple 2D model. Preliminary mesh near the contact area during the period between the 6th and 7th frames in Fig. 8. The checkerboard coloring is for differentiating between the NURBS elements. A band of elements are colored blue to illustrate the mesh rotation. (Color figure online)

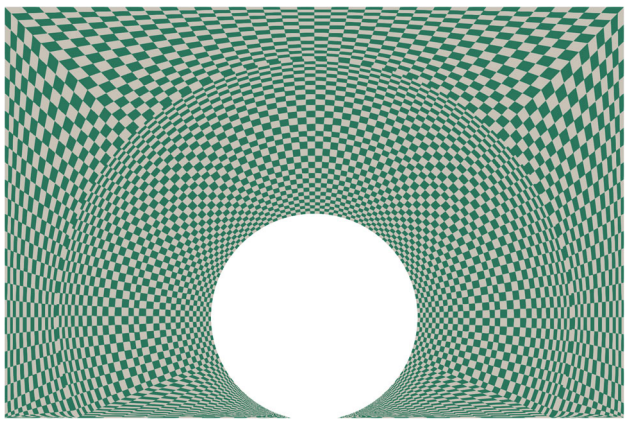

Fig. 10 A simple 2D model. Refined mesh. The number of control points and elements are 7992 and 7200. The checkerboard coloring is for differentiating between the NURBS elements

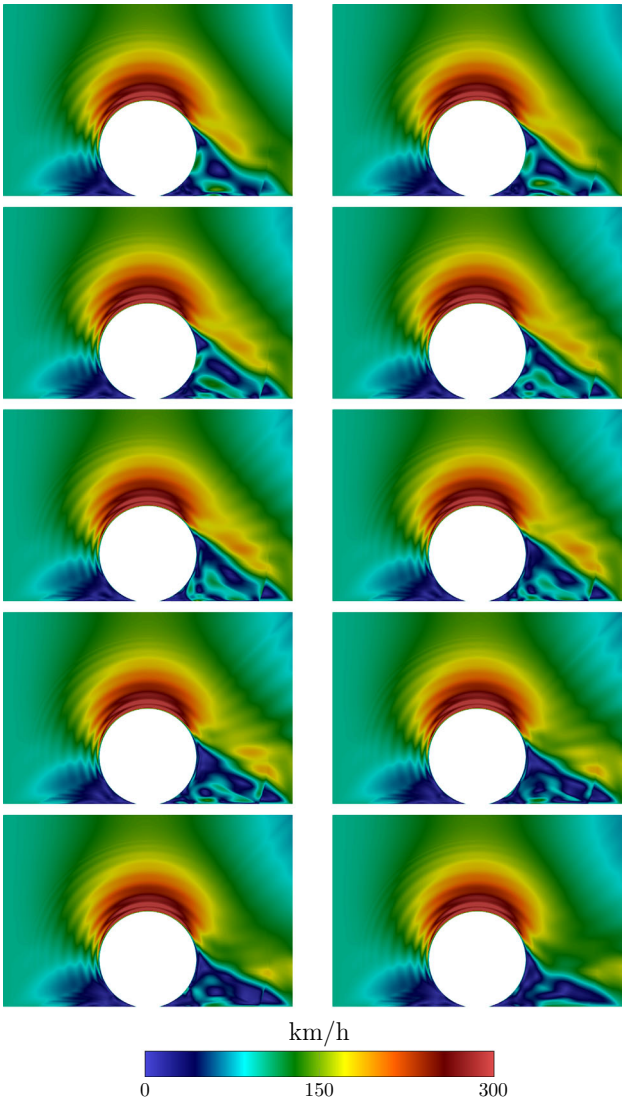

Fig. 11 A simple 2D model. Velocity magnitude from the preliminary-mesh computation with the nonmoving-mesh (ST-SI-IGA) method, at 10 uniformly spaced instants during a full rotation

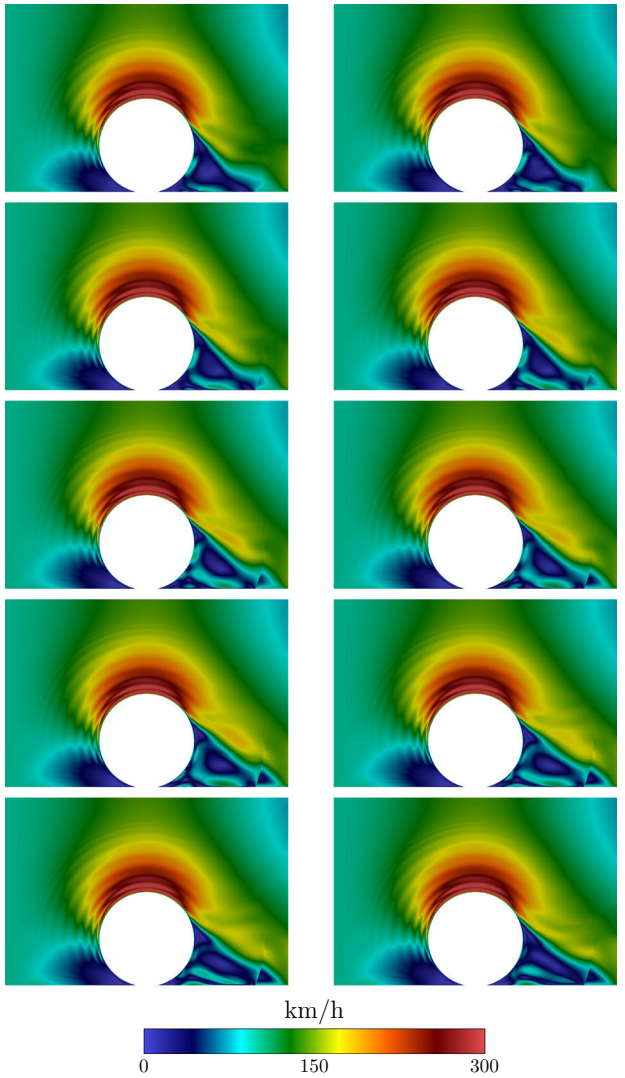

Fig. 12 A simple 2D model. Velocity magnitude from the preliminary-mesh computation with the ST-SI-TC-IGA method, at the same instants as in Fig. 11

5 Tire aerodynamics with an actual tire geometry

We present a tire-aerodynamics computational analysis with an actual tire geometry. The tire has a prescribed motion, is in contact with the road, and has a prescribed deformation.

5.1 Problem setup

The tire model is shown in Fig. 16. The diameter and width are 1.03 m and 260 mm. There are three longitudinal grooves, and a transverse groove for every 5°. The depth and width of the grooves are 11.071 mm and 11.692 mm for the center groove, 10.974 mm and 7.177 mm for the side grooves, and

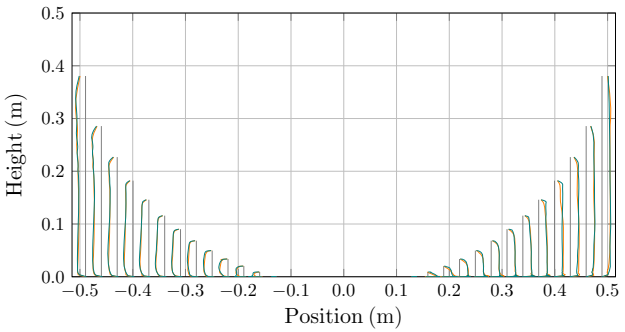

Fig. 13 A simple 2D model. Horizontal component of the flow velocity relative to the planar surface, displayed along vertical lines at different positions from the center contact point. Computed with the nonmoving-mesh (ST-SI-IGA) method, using the preliminary (orange) and refined (green) meshes. (Color figure online)

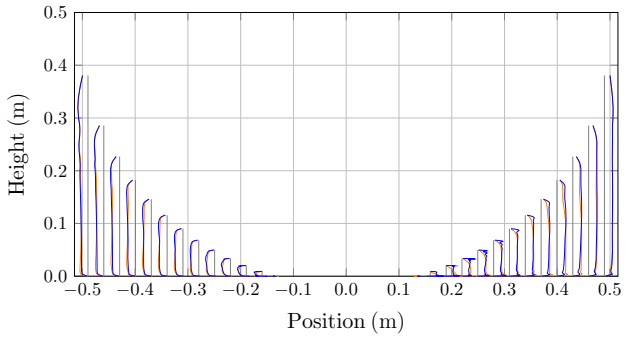

Fig. 14 A simple 2D model. Horizontal component of the flow velocity relative to the planar surface, displayed along vertical lines at different positions from the center contact point. Computed with the nonmoving-mesh (ST-SI-IGA) (orange) and ST-SI-TC-IGA (blue) methods, using the preliminary mesh. (Color figure online)

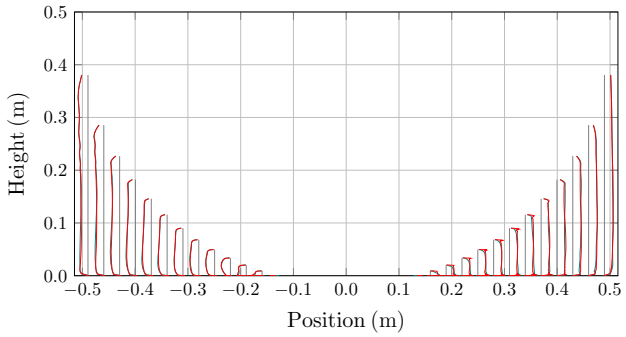

Fig. 15 A simple 2D model. Horizontal component of the flow velocity relative to the planar surface, displayed along vertical lines at different positions from the center contact point. Computed with the nonmoving-mesh (ST-SI-IGA) (green) and ST-SI-TC-IGA (red) methods, using the refined mesh. (Color figure online)

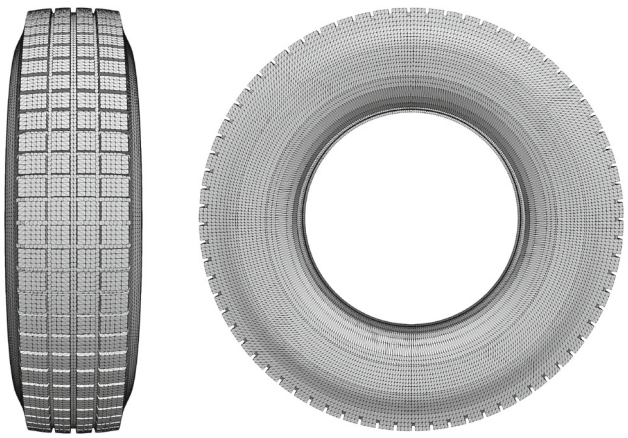

Fig. 16 Tire aerodynamics with an actual tire geometry. Tire model

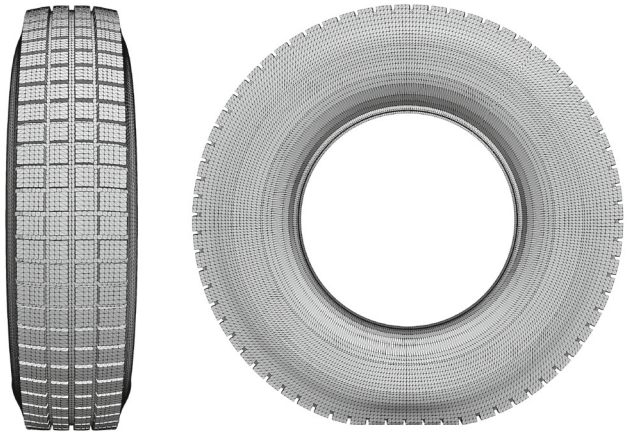

Fig. 17 Tire aerodynamics with an actual tire geometry. Deformed shape

11.085 mm and 8.489 mm for the transverse grooves. Tire with the prescribed deformation is shown in Fig. 17.

The tire deformation is represented in time based on the deformation at five instants of a 5° rotation, which was provided by the tire company. Figure 18 shows the tire deformation at those five instants. The deformation representation in time is with cubic NURBS basis functions and obtained by projection from the five-instant data. The projection is done with the ST-C [105]. The rotation speed corresponds to a linear speed of 103 km/h at the undeformed tire periphery. In this case, $U_0 = 100$ km/h. The density and kinematic viscosity of the air are $1.205\,\mathrm{kg/m^3}$ and $1.511 \times 10^{-5}\,\mathrm{m^2/s}$.

5.2 Computational domain, boundary conditions and meshes

The computational domain is shown in Fig. 19. The domain size is 4.000 m and 5.489 m in width and height, and 8.000 m in the flow direction. The tire is placed at 2.000 m from the inflow boundary. The boundary conditions are 3D extensions of the conditions in the simple 2D model, with slip conditions on the boundary planes perpendicular to the tire axis. We use two different quadratic NURBS meshes: a preliminary mesh and a refined mesh. The number of control points and elements for the two meshes are given in Table 1.

Figure 20 shows, for the two meshes, the refinement level near the tire surface. As can be discerned from the figure, the refined mesh has twice the resolution in the normal direction, and four times the resolution in the longitudinal direction. In the transverse direction, it has four times the resolution across the treads, and twice the resolution across the grooves. We note that most of the mesh generation complexity is near the tire surfaces, which we wanted to do manually. The rest of the mesh could have been generated automatically (see [96]), but that was also generated manually, because it was not that difficult.

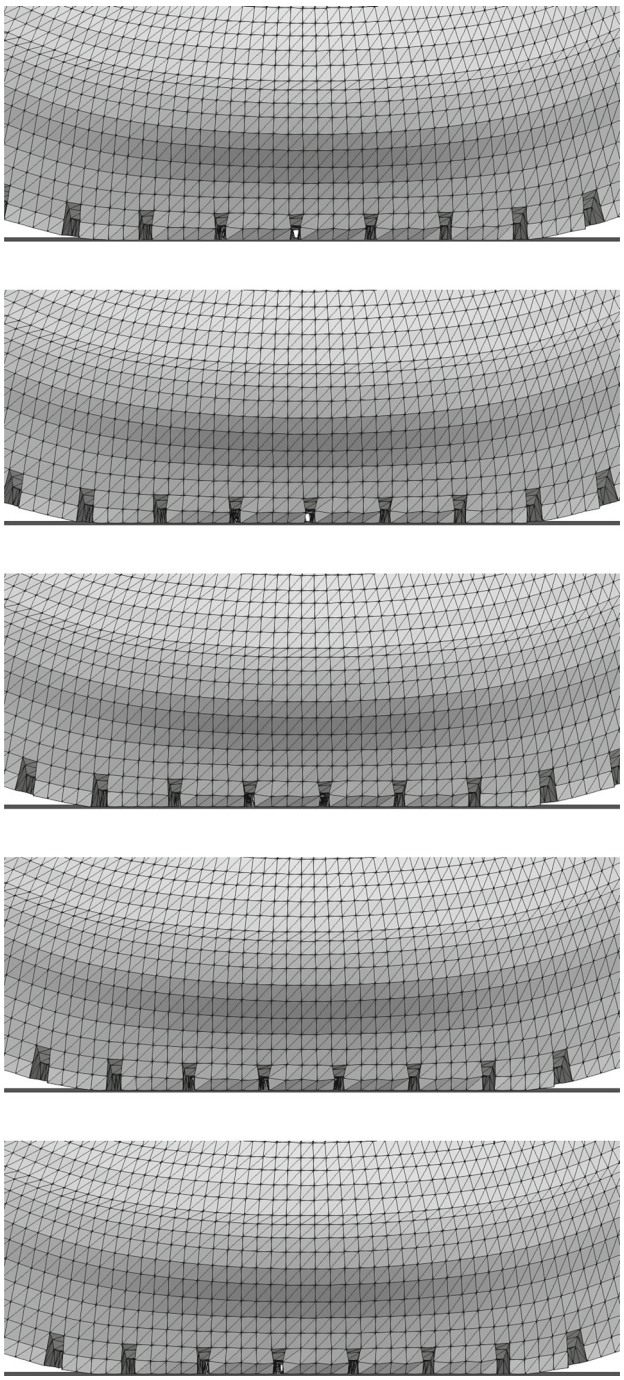

Fig. 18 Tire aerodynamics with an actual tire geometry. Tire deformation near the contact region at five instants of a 5° rotation, provided by the tire company

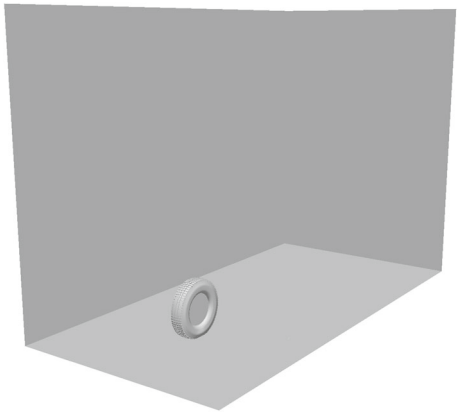

Fig. 19 Tire aerodynamics with an actual tire geometry. Computational domain

Table 1 Tire aerodynamics with an actual tire geometry. Number of control points (nc) and elements (ne) for the two quadratic NURBS meshes used in the computations

	Preliminary	Refined
nc	690,144	4,149,720
ne	376,560	2,921,552

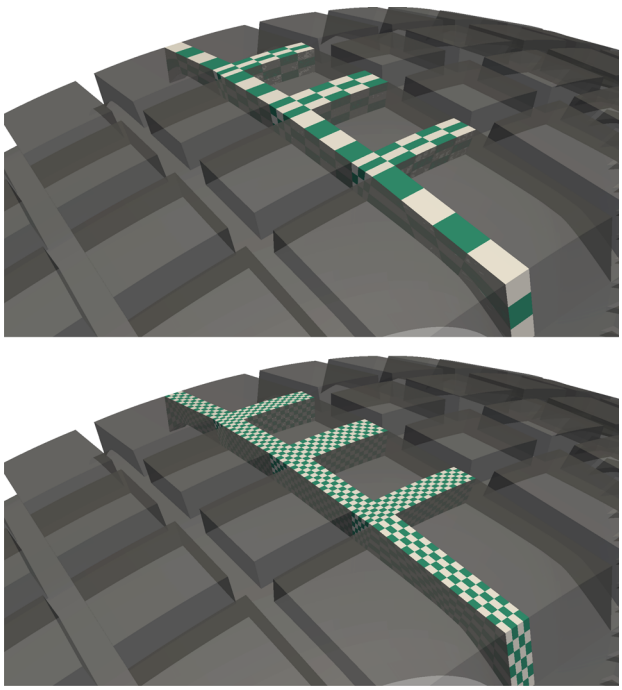

Fig. 20 Tire aerodynamics with an actual tire geometry. Refinement level near the tire surface for the preliminary (top) and refined (bottom) meshes. The checkerboard coloring is for differentiating between the NURBS elements

5.3 Computational conditions

In the computation with the preliminary mesh, there are 1440 time steps per rotation, which is equivalent to a time-step size of 7.85×10^{-5} s. In the refined-mesh computation, the time-step size is reduced to one-fourth of the value used with the preliminary mesh, making it 1.96×10^{-5} s. The number of nonlinear iterations per time step is 3, and the number of GMRES iterations per nonlinear iteration is 300.

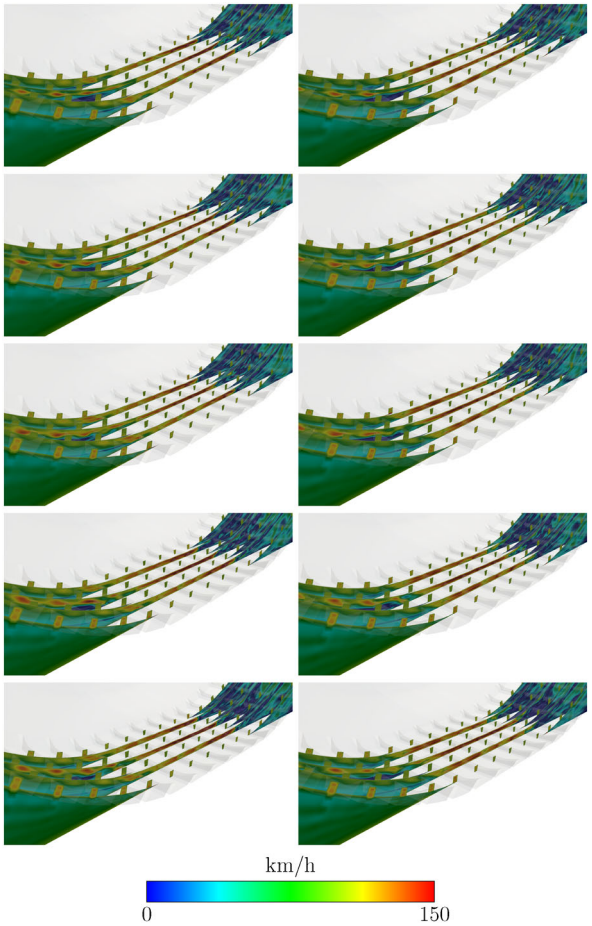

Fig. 21 Tire aerodynamics with an actual tire geometry. Computed with the preliminary mesh. Velocity magnitude near the contact area, displayed on planes perpendicular to the tire axis

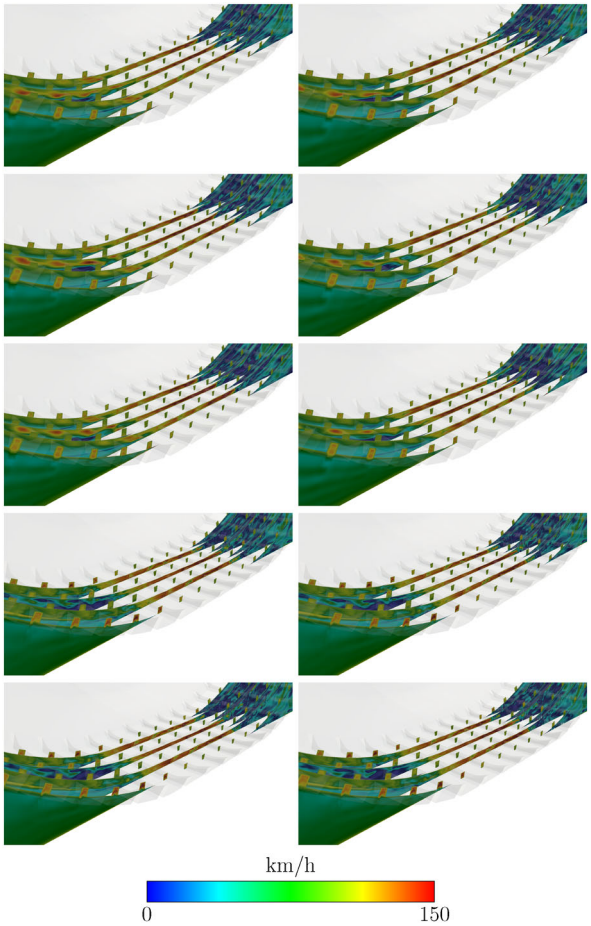

Fig. 22 Tire aerodynamics with an actual tire geometry. Computed with the refined mesh. Velocity magnitude near the contact area, displayed on planes perpendicular to the tire axis

5.4 Results

Figures 21 and 22 show, for the two meshes, the velocity magnitude near the contact area. In the solution obtained with the preliminary mesh, the flow patterns are closer to the tire surface. Figures 23 and 24 show, for the two meshes, the isosurfaces corresponding to a positive value of the second invariant of the velocity gradient tensor, colored by the velocity magnitude. The solution obtained with the refined mesh has a better resolution of the vortex structure. This confirms the importance of having a good method and high resolution near the tire–road contact areas.

6 Concluding remarks

We have successfully addressed the computational challenges faced in tire aerodynamics with actual geometry, road contact and tire deformation. The challenges include (1) the complexity of an actual tire geometry with longitudinal and transverse grooves, (2) the spin of the tire, (3) maintaining accurate representation of the boundary layers near the tire while being able to deal with the flow-domain topology change created by the road contact and tire deformation, and (4) the turbulent nature of the flow. The ST-SI-TC-IGA, a new ST computational method, has enabled us to overcome these challenges. The core component of the ST-SI-TC-IGA is the ST-VMS, and the other key components are the ST-SI, ST-TC and ST-IGA. The challenge created by the turbulent nature of the flow is addressed with the VMS feature of the ST-VMS. The moving-mesh feature of the ST framework enables high-resolution flow computation near the air–tire interfaces as the tire rotates. These two features are enhanced with the higher-order accuracy of the ST framework. With the ST-SI, we are able to do moving-mesh computations with the tire spinning. The mesh covering the tire spins with it, and the SI between the spinning mesh and the rest of the mesh accurately connects the two sides of the solution. With the ST-TC, we are able to do moving-mesh computations even with the TC created by the contact between the tire and the

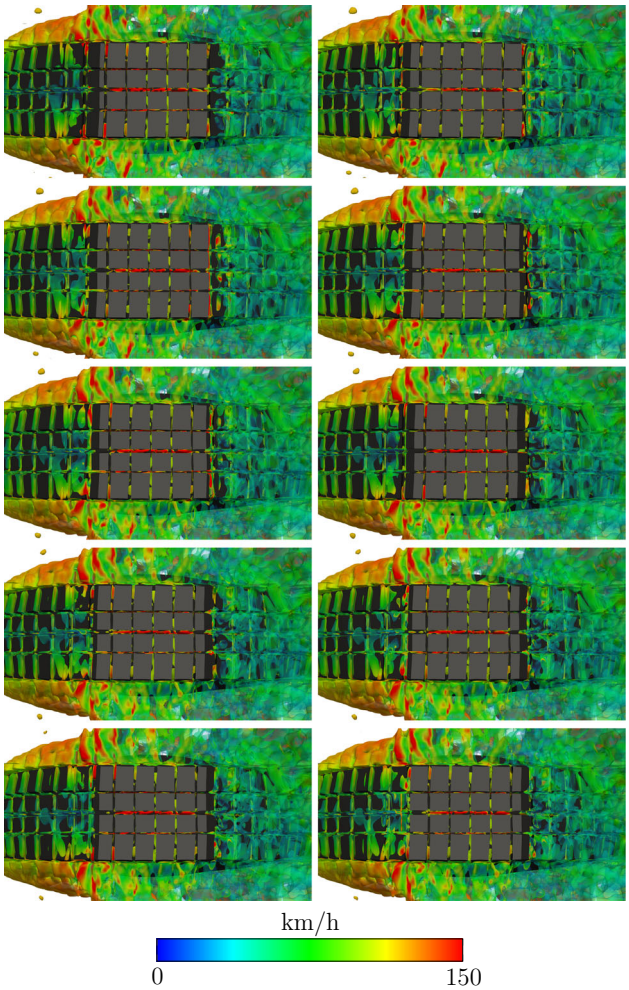

Fig. 23 Tire aerodynamics with an actual tire geometry. Computed with the preliminary mesh. Isosurfaces corresponding to a positive value of the second invariant of the velocity gradient tensor, colored by the velocity magnitude, viewed from the bottom. The gray zones are the contact areas

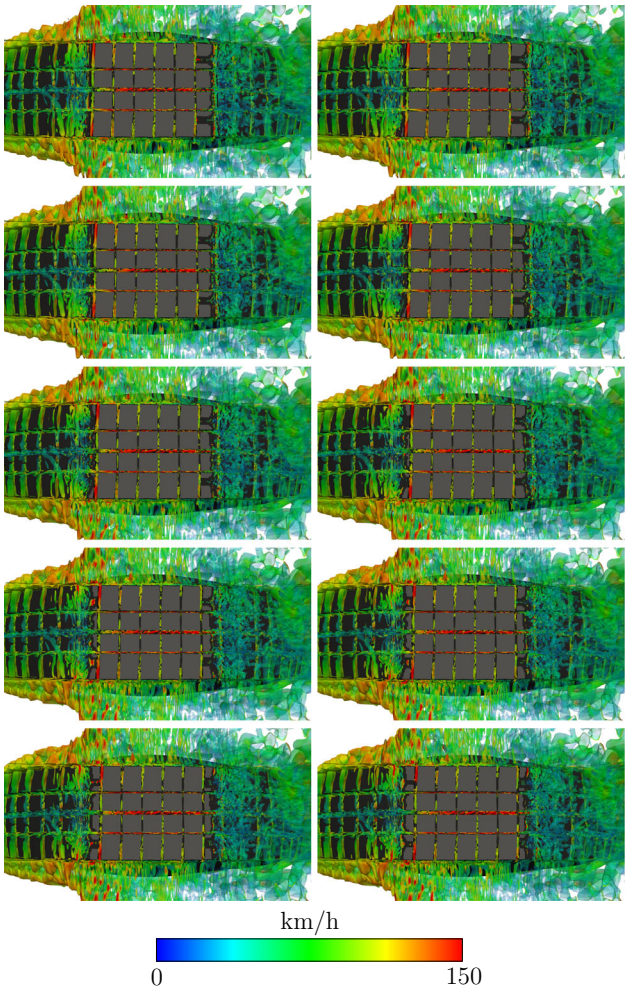

Fig. 24 Tire aerodynamics with an actual tire geometry. Computed with the refined mesh. Isosurfaces corresponding to a positive value of the second invariant of the velocity gradient tensor, colored by the velocity magnitude, viewed from the bottom. The gray zones are the contact areas

road. This enables dealing with the contact while maintaining high-resolution flow representation near the tire. Integration of the ST-SI and ST-TC enables high-resolution flow representation even though parts of the SI are coinciding with the tire and road surfaces. It also enables dealing with the tire–road contact location change and contact sliding. Integration of the ST-IGA with the ST-SI and ST-TC not only enables a more accurate representation of the tire geometry and increased accuracy in the flow solution, but also keeps the element density in the tire grooves and in the narrow spaces near the contact areas at a reasonable level. We presented computations with two models of flow around a rotating tire with road contact and prescribed deformation. One is a simple 2D model for verification purposes, and one is a 3D model with an actual tire geometry and a deformation pattern provided by the tire company. The 2D computations confirm the reliability of the moving-mesh and TC features of the ST-SI-TC-IGA. The 3D computations confirm the importance of having a good method and high resolution near the tire–road contact areas. Overall, the computations show the effectiveness of the ST-SI-TC-IGA in tire aerodynamics.

Acknowledgements This work was supported (first and second authors) in part by Grant-in-Aid for Challenging Exploratory Research 16K13779 from JSPS; Grant-in-Aid for Scientific Research (S) 26220002 from the Ministry of Education, Culture, Sports, Science and Technology of Japan (MEXT); and Rice–Waseda research agreement. This work was also supported (first author) in part by Grant-in-Aid for JSPS Research Fellow 17J10893. The computational method parts of the work were also supported (third author) in part by ARO Grant W911NF-17-1-0046 and Top Global University Project of Waseda University. The tire deformation used in Sect. 5 was provided by Bridgestone.

A Element metric tensor

Here we provide from [98,103] the element metric tensor in space and in the ST framework. To obtain the element length and stabilization parameters, we use the metric tensor in the space and also in the ST framework.

A.1 Element metric tensor in space

Components of the Jacobian matrix $\mathbf{Q}$ are written as

$$Q_{ij} = \frac{\partial x_i}{\partial \xi_j}, \tag{19}$$

where ξ_j is the parametric coordinate in jth direction. We first scale it with a matrix $\mathbf{D}$ to take into account the polynomial order or other factors such as the dimensions of the element domain in the parametric space:

$$\hat{\mathbf{Q}} = \mathbf{Q}\mathbf{D}^{-1}. \tag{20}$$

With this vector, we define the element length as

$$h_{\mathrm{RQD}} = 2\left(\mathbf{rr} : \mathbf{G}\right)^{-\frac{1}{2}}. \tag{21}$$

where

$$\mathbf{G} = \hat{\mathbf{Q}}^{-T}\hat{\mathbf{Q}}^{-1}. \tag{22}$$

Remark 4 What we get with $\mathbf{D} = \mathbf{I}$ has been used in many methods of calculating the stabilization parameters (see, for example, [23]). In those methods, a scaling factor taking the polynomial order into account is applied to the element length, and here we do the scaling in the parametric space, for each of the parametric directions.

Sweeping over all the directions represented by $\mathbf{r}$, we obtain the minimum and maximum element lengths:

$$h_{\mathrm{MIN}} \equiv 2 \min_{\mathbf{r}} \left(\left(\mathbf{rr} : \mathbf{G}\right)^{-\frac{1}{2}}\right), \tag{23}$$

$$h_{\mathrm{MAX}} \equiv 2 \max_{\mathbf{r}} \left(\left(\mathbf{rr} : \mathbf{G}\right)^{-\frac{1}{2}}\right). \tag{24}$$

They are equivalent to

$$h_{\mathrm{MIN}} = 2\left(\max_{\mathbf{r}} \left(\mathbf{rr} : \mathbf{G}\right)\right)^{-\frac{1}{2}}, \tag{25}$$

$$= 2\left(\lambda_{\max}\left(\mathbf{G}\right)\right)^{-\frac{1}{2}}, \tag{26}$$

and

$$h_{\mathrm{MAX}} = 2\left(\min_{\mathbf{r}} \left(\mathbf{rr} : \mathbf{G}\right)\right)^{-\frac{1}{2}}, \tag{27}$$

$$= 2\left(\lambda_{\min}\left(\mathbf{G}\right)\right)^{-\frac{1}{2}}, \tag{28}$$

where $\lambda_{\max}$ and $\lambda_{\min}$ are the maximum and minimum eigenvalues of the argument matrix.

Remark 5 In the implementation, we take measures to keep the calculated element length between h_{MIN} and h_{MAX}.

A.2 Element metric tensor in the ST framework

The ST Jacobian matrix is

$$\mathbf{Q}^{\mathrm{ST}} = \begin{bmatrix} \frac{\partial t}{\partial \theta} & \frac{\partial t}{\partial \boldsymbol{\xi}} \\ \frac{\partial \mathbf{x}}{\partial \theta} & \mathbf{Q} \end{bmatrix} \tag{29}$$

$$= \begin{bmatrix} \frac{\partial t}{\partial \theta} & \frac{\partial t}{\partial \boldsymbol{\xi}} \\ \mathbf{v}\frac{\partial t}{\partial \theta} & \mathbf{Q} \end{bmatrix}, \tag{30}$$

where θ is the parametric coordinate in time, and $\mathbf{v}$ is the mesh velocity:

$$\mathbf{v} = \left.\frac{\partial \mathbf{x}}{\partial t}\right|_{\boldsymbol{\xi}}. \tag{31}$$

The ST scaling matrix is given as

$$\mathbf{D}^{\mathrm{ST}} = \begin{bmatrix} D_\theta & \mathbf{0}^T \\ \mathbf{0} & \mathbf{D} \end{bmatrix}, \tag{32}$$

and the scaling becomes

$$\hat{\mathbf{Q}}^{\mathrm{ST}} = \mathbf{Q}^{\mathrm{ST}}\left(\mathbf{D}^{\mathrm{ST}}\right)^{-1}. \tag{33}$$

The ST metric tensor is defined as

$$\mathbf{G}^{\mathrm{ST}} = \left(\hat{\mathbf{Q}}^{\mathrm{ST}}\right)^{-T}\left(\hat{\mathbf{Q}}^{\mathrm{ST}}\right)^{-1}. \tag{34}$$

References

1. Kuraishi T, Takizawa K, Tezduyar TE (2018) Space–time computational analysis of tire aerodynamics with actual geometry, road contact and tire deformation. In: Tezduyar TE (ed) Frontiers in computational fluid–structure interaction and flow simulation: research from lead investigators under forty—2018. Modeling and Simulation in Science, Engineering and Technology, pp 333–371. Springer, Berlin. ISBN: 978-3-319-96468-3. https://doi.org/10.1007/978-3-319-96469-0_8
2. Takizawa K, Tezduyar TE, Terahara T, Sasaki T (2017) Heart valve flow computation with the integrated space–time VMS, slip interface, topology change and isogeometric discretization

methods. Comput Fluids 158:176–188. https://doi.org/10.1016/j.compfluid.2016.11.012
3. Takizawa K, Tezduyar TE (2011) Multiscale space-time fluid-structure interaction techniques. Comput Mech 48:247–267. https://doi.org/10.1007/s00466-011-0571-z
4. Takizawa K, Tezduyar TE (2012) Space-time fluid-structure interaction methods. Math Models Methods Appl Sci 22(supp02):1230001. https://doi.org/10.1142/S0218202512300013
5. Takizawa K, Tezduyar TE, Kuraishi T (2015) Multiscale ST methods for thermo-fluid analysis of a ground vehicle and its tires. Math Models Methods Appl Sci 25:2227–2255. https://doi.org/10.1142/S0218202515400072
6. Takizawa K, Tezduyar TE, Mochizuki H, Hattori H, Mei S, Pan L, Montel K (2015) Space-time VMS method for flow computations with slip interfaces (ST-SI). Math Models Methods Appl Sci 25:2377–2406. https://doi.org/10.1142/S0218202515400126
7. Takizawa K, Tezduyar TE, Kuraishi T, Tabata S, Takagi H (2016) Computational thermo-fluid analysis of a disk brake. Comput Mech 57:965–977. https://doi.org/10.1007/s00466-016-1272-4
8. Takizawa K, Tezduyar TE, Buscher A, Asada S (2014) Space–time interface-tracking with topology change (ST-TC). Comput Mech 54:955–971. https://doi.org/10.1007/s00466-013-0935-7
9. Takizawa K, Tezduyar TE, Buscher A, Asada S (2014) Space–time fluid mechanics computation of heart valve models. Comput Mech 54:973–986. https://doi.org/10.1007/s00466-014-1046-9
10. Takizawa K, Henicke B, Puntel A, Spielman T, Tezduyar TE (2012) Space–time computational techniques for the aerodynamics of flapping wings. J Appl Mech 79:010903. https://doi.org/10.1115/1.4005073
11. Takizawa K, Tezduyar TE, Otoguro Y, Terahara T, Kuraishi T, Hattori H (2017) Turbocharger flow computations with the space–time isogeometric analysis (ST-IGA). Comput Fluids 142:15–20. https://doi.org/10.1016/j.compfluid.2016.02.021
12. Tezduyar TE (1992) Stabilized finite element formulations for incompressible flow computations. Adv Appl Mech 28:1–44. https://doi.org/10.1016/S0065-2156(08)70153-4
13. Tezduyar TE (2003) Computation of moving boundaries and interfaces and stabilization parameters. Int J Numer Methods Fluids 43:555–575. https://doi.org/10.1002/fld.505
14. Tezduyar TE, Sathe S (2007) Modeling of fluid-structure interactions with the space–time finite elements: solution techniques. Int J Numer Methods Fluids 54:855–900. https://doi.org/10.1002/fld.1430
15. Brooks AN, Hughes TJR (1982) Streamline upwind/Petrov–Galerkin formulations for convection dominated flows with particular emphasis on the incompressible Navier–Stokes equations. Comput Methods Appl Mech Eng 32:199–259
16. Hughes TJR (1995) Multiscale phenomena: Green's functions, the Dirichlet-to-Neumann formulation, subgrid scale models, bubbles, and the origins of stabilized methods. Comput Methods Appl Mech Eng 127:387–401
17. Hughes TJR, Oberai AA, Mazzei L (2001) Large eddy simulation of turbulent channel flows by the variational multiscale method. Phys Fluids 13:1784–1799
18. Bazilevs Y, Calo VM, Cottrell JA, Hughes TJR, Reali A, Scovazzi G (2007) Variational multiscale residual-based turbulence modeling for large eddy simulation of incompressible flows. Comput Methods Appl Mech Eng 197:173–201
19. Bazilevs Y, Akkerman I (2010) Large eddy simulation of turbulent Taylor–Couette flow using isogeometric analysis and the residual-based variational multiscale method. J Comput Phys 229:3402–3414
20. Bazilevs Y, Calo VM, Hughes TJR, Zhang Y (2008) Isogeometric fluid-structure interaction: theory, algorithms, and computations. Comput Mech 43:3–37
21. Takizawa K, Bazilevs Y, Tezduyar TE (2012) Space-time and ALE-VMS techniques for patient-specific cardiovascular fluid-structure interaction modeling. Arch Comput Methods Eng 19:171–225. https://doi.org/10.1007/s11831-012-9071-3
22. Bazilevs Y, Hsu M-C, Takizawa K, Tezduyar TE (2012) ALE-VMS and ST-VMS methods for computer modeling of wind-turbine rotor aerodynamics and fluid-structure interaction. Math Models Methods Appl Sci 22(supp02):1230002. https://doi.org/10.1142/S0218202512300025
23. Bazilevs Y, Takizawa K, Tezduyar TE (2013) Computational fluid–structure interaction: methods and applications. Wiley. ISBN: 978-0470978771
24. Bazilevs Y, Takizawa K, Tezduyar TE (2013) Challenges and directions in computational fluid-structure interaction. Math Models Methods Appl Sci 23:215–221. https://doi.org/10.1142/S0218202513400010
25. Bazilevs Y, Takizawa K, Tezduyar TE (2015) New directions and challenging computations in fluid dynamics modeling with stabilized and multiscale methods. Math Models Methods Appl Sci 25:2217–2226. https://doi.org/10.1142/S0218202515020029
26. Kalro V, Tezduyar TE (2000) A parallel 3D computational method for fluid-structure interactions in parachute systems. Comput Methods Appl Mech Eng 190:321–332. https://doi.org/10.1016/S0045-7825(00)00204-8
27. Bazilevs Y, Hughes TJR (2007) Weak imposition of Dirichlet boundary conditions in fluid mechanics. Comput Fluids 36:12–26
28. Bazilevs Y, Michler C, Calo VM, Hughes TJR (2010) Isogeometric variational multiscale modeling of wall-bounded turbulent flows with weakly enforced boundary conditions on unstretched meshes. Comput Methods Appl Mech Eng 199:780–790
29. Hsu M-C, Akkerman I, Bazilevs Y (2012) Wind turbine aerodynamics using ALE-VMS: validation and role of weakly enforced boundary conditions. Comput Mech 50:499–511
30. Bazilevs Y, Hughes TJR (2008) NURBS-based isogeometric analysis for the computation of flows about rotating components. Comput Mech 43:143–150
31. Hsu M-C, Bazilevs Y (2012) Fluid-structure interaction modeling of wind turbines: simulating the full machine. Comput Mech 50:821–833
32. Moghadam ME, Bazilevs Y, Hsia T-Y, Vignon-Clementel IE, Marsden AL (2011) The modeling of congenital hearts alliance (MOCHA) A comparison of outlet boundary treatments for prevention of backflow divergence with relevance to blood flow simulations. Comput Mech 48:277–291. https://doi.org/10.1007/s00466-011-0599-0
33. Bazilevs Y, Hsu M-C, Akkerman I, Wright S, Takizawa K, Henicke B, Spielman T, Tezduyar TE (2011) 3D simulation of wind turbine rotors at full scale. Part I: geometry modeling and aerodynamics. Int J Numer Methods Fluids 65:207–235. https://doi.org/10.1002/fld.2400
34. Bazilevs Y, Hsu M-C, Kiendl J, Wüchner R, Bletzinger K-U (2011) 3D simulation of wind turbine rotors at full scale. Part II: fluid-structure interaction modeling with composite blades. Int J Numer Methods Fluids 65:236–253
35. Hsu M-C, Akkerman I, Bazilevs Y (2011) High-performance computing of wind turbine aerodynamics using isogeometric analysis. Comput Fluids 49:93–100
36. Bazilevs Y, Hsu M-C, Scott MA (2012) Isogeometric fluid-structure interaction analysis with emphasis on non-matching discretizations, and with application to wind turbines. Comput Methods Appl Mech Eng 249–252:28–41
37. Hsu M-C, Akkerman I, Bazilevs Y (2014) Finite element simulation of wind turbine aerodynamics: validation study using NREL phase VI experiment. Wind Energy 17:461–481

38. Korobenko A, Hsu M-C, Akkerman I, Tippmann J, Bazilevs Y (2013) Structural mechanics modeling and FSI simulation of wind turbines. Math Models Methods Appl Sci 23:249–272
39. Bazilevs Y, Takizawa K, Tezduyar TE, Hsu M-C, Kostov N, McIntyre S (2014) Aerodynamic and FSI analysis of wind turbines with the ALE-VMS and ST-VMS methods. Arch Comput Methods Eng 21:359–398. https://doi.org/10.1007/s11831-014-9119-7
40. Bazilevs Y, Korobenko A, Deng X, Yan J (2015) Novel structural modeling and mesh moving techniques for advanced FSI simulation of wind turbines. Int J Numer Methods Eng 102:766–783. https://doi.org/10.1002/nme.4738
41. Korobenko A, Hsu M-C, Akkerman I, Bazilevs Y (2013) Aerodynamic simulation of vertical-axis wind turbines. J Appl Mech 81:021011. https://doi.org/10.1115/1.4024415
42. Bazilevs Y, Korobenko A, Deng X, Yan J, Kinzel M, Dabiri JO (2014) FSI modeling of vertical-axis wind turbines. J Appl Mech 81:081006. https://doi.org/10.1115/1.4027466
43. Yan J, Korobenko A, Deng X, Bazilevs Y (2016) Computational free-surface fluid-structure interaction with application to floating offshore wind turbines. Comput Fluids 141:155–174. https://doi.org/10.1016/j.compfluid.2016.03.008
44. Bazilevs Y, Korobenko A, Yan J, Pal A, Gohari SMI, Sarkar S (2015) ALE-VMS formulation for stratified turbulent incompressible flows with applications. Math Models Methods Appl Sci 25:2349–2375. https://doi.org/10.1142/S0218202515400114
45. Bazilevs Y, Korobenko A, Deng X, Yan J (2016) FSI modeling for fatigue-damage prediction in full-scale wind-turbine blades. J Appl Mech 83(6):061010
46. Bazilevs Y, Calo VM, Zhang Y, Hughes TJR (2006) Isogeometric fluid-structure interaction analysis with applications to arterial blood flow. Comput Mech 38:310–322
47. Bazilevs Y, Gohean JR, Hughes TJR, Moser RD, Zhang Y (2000) Patient-specific isogeometric fluid-structure interaction analysis of thoracic aortic blood flow due to implantation of the Jarvik 2000 left ventricular assist device. Comput Methods Appl Mech Eng 198(2009):3534–3550
48. Bazilevs Y, Hsu M-C, Benson D, Sankaran S, Marsden A (2009) Computational fluid-structure interaction: methods and application to a total cavopulmonary connection. Comput Mech 45:77–89
49. Bazilevs Y, Hsu M-C, Zhang Y, Wang W, Liang X, Kvamsdal T, Brekken R, Isaksen J (2010) A fully-coupled fluid-structure interaction simulation of cerebral aneurysms. Comput Mech 46:3–16
50. Bazilevs Y, Hsu M-C, Zhang Y, Wang W, Kvamsdal T, Hentschel S, Isaksen J (2010) Computational fluid-structure interaction: methods and application to cerebral aneurysms. Biomech Model Mechanobiol 9:481–498
51. Hsu M-C, Bazilevs Y (2011) Blood vessel tissue prestress modeling for vascular fluid-structure interaction simulations. Finite Elements Anal Des 47:593–599
52. Long CC, Marsden AL, Bazilevs Y (2013) Fluid-structure interaction simulation of pulsatile ventricular assist devices. Comput Mech 52:971–981. https://doi.org/10.1007/s00466-013-0858-3
53. Long CC, Esmaily-Moghadam M, Marsden AL, Bazilevs Y (2014) Computation of residence time in the simulation of pulsatile ventricular assist devices. Comput Mech 54:911–919. https://doi.org/10.1007/s00466-013-0931-y
54. Long CC, Marsden AL, Bazilevs Y (2014) Shape optimization of pulsatile ventricular assist devices using FSI to minimize thrombotic risk. Comput Mech 54:921–932. https://doi.org/10.1007/s00466-013-0967-z
55. Hsu M-C, Kamensky D, Bazilevs Y, Sacks MS, Hughes TJR (2014) Fluid-structure interaction analysis of bioprosthetic heart valves: significance of arterial wall deformation. Comput Mech 54:1055–1071. https://doi.org/10.1007/s00466-014-1059-4
56. Hsu M-C, Kamensky D, Xu F, Kiendl J, Wang C, Wu MCH, Mineroff J, Reali A, Bazilevs Y, Sacks MS (2015) Dynamic and fluid-structure interaction simulations of bioprosthetic heart valves using parametric design with T-splines and Fung-type material models. Comput Mech 55:1211–1225. https://doi.org/10.1007/s00466-015-1166-x
57. Kamensky D, Hsu M-C, Schillinger D, Evans JA, Aggarwal A, Bazilevs Y, Sacks MS, Hughes TJR (2015) An immersogeometric variational framework for fluid-structure interaction: application to bioprosthetic heart valves. Comput Methods Appl Mech Eng 284:1005–1053
58. Akkerman I, Bazilevs Y, Benson DJ, Farthing MW, Kees CE (2012) Free-surface flow and fluid-object interaction modeling with emphasis on ship hydrodynamics. J Appl Mech 79:010905
59. Akkerman I, Dunaway J, Kvandal J, Spinks J, Bazilevs Y (2012) Toward free-surface modeling of planing vessels: simulation of the Fridsma hull using ALE-VMS. Comput Mech 50:719–727
60. Wang C, Wu MCH, Xu F, Hsu M-C, Bazilevs Y (2017) Modeling of a hydraulic arresting gear using fluid-structure interaction and isogeometric analysis. Comput Fluids 142:3–14. https://doi.org/10.1016/j.compfluid.2015.12.004
61. Wu MCH, Kamensky D, Wang C, Herrema AJ, Xu F, Pigazzini MS, Verma A, Marsden AL, Bazilevs Y, Hsu M-C (2017)Optimizing fluid–structure interaction systems with immersogeometric analysis and surrogate modeling: application to a hydraulic arresting gear. Comput Methods Appl Mech Eng (2017). https://doi.org/10.1016/j.cma.2016.09.032.
62. Yan J, Deng X, Korobenko A, Bazilevs Y (2017) Free-surface flow modeling and simulation of horizontal-axis tidal-stream turbines. Comput Fluids 158:157–166. https://doi.org/10.1016/j.compfluid.2016.06.016
63. Augier B, Yan J, Korobenko A, Czarnowski J, Ketterman G, Bazilevs Y (2015) Experimental and numerical FSI study of compliant hydrofoils. Comput Mech 55:1079–1090. https://doi.org/10.1007/s00466-014-1090-5
64. Yan J, Augier B, Korobenko A, Czarnowski J, Ketterman G, Bazilevs Y (2016) FSI modeling of a propulsion system based on compliant hydrofoils in a tandem configuration. Comput Fluids 141:201–211. https://doi.org/10.1016/j.compfluid.2015.07.013
65. Takizawa K, Tezduyar TE (2012) Computational methods for parachute fluid-structure interactions. Arch Comput Methods Eng 19:125–169. https://doi.org/10.1007/s11831-012-9070-4
66. Takizawa K, Fritze M, Montes D, Spielman T, Tezduyar TE (2012) Fluid-structure interaction modeling of ringsail parachutes with disreefing and modified geometric porosity. Comput Mech 50:835–854. https://doi.org/10.1007/s00466-012-0761-3
67. Takizawa K, Tezduyar TE, Boben J, Kostov N, Boswell C, Buscher A (2013) Fluid-structure interaction modeling of clusters of spacecraft parachutes with modified geometric porosity. Comput Mech 52:1351–1364. https://doi.org/10.1007/s00466-013-0880-5
68. Takizawa K, Tezduyar TE, Boswell C, Tsutsui Y, Montel K (2015) Special methods for aerodynamic-moment calculations from parachute FSI modeling. Comput Mech 55:1059–1069. https://doi.org/10.1007/s00466-014-1074-5
69. Takizawa K, Montes D, Fritze M, McIntyre S, Boben J, Tezduyar TE (2013) Methods for FSI modeling of spacecraft parachute dynamics and cover separation. Math Models Methods Appl Sci 23:307–338. https://doi.org/10.1142/S0218202513400058
70. Takizawa K, Tezduyar TE, Boswell C, Kolesar R, Montel K (2014) FSI modeling of the reefed stages and disreefing of the Orion spacecraft parachutes. Comput Mech 54:1203–1220. https://doi.org/10.1007/s00466-014-1052-y
71. Takizawa K, Tezduyar TE, Kolesar R, Boswell C, Kanai T, Montel K (2014) Multiscale methods for gore curvature calculations from FSI modeling of spacecraft parachutes. Comput Mech 54:1461–1476. https://doi.org/10.1007/s00466-014-1069-2

72. Takizawa K, Tezduyar TE, Kolesar R (2015) FSI modeling of the Orion spacecraft drogue parachutes. Comput Mech 55:1167–1179. https://doi.org/10.1007/s00466-014-1108-z
73. Takizawa K, Henicke B, Tezduyar TE, Hsu M-C, Bazilevs Y (2011) Stabilized space–time computation of wind-turbine rotor aerodynamics. Comput Mech 48:333–344. https://doi.org/10.1007/s00466-011-0589-2
74. Takizawa K, Henicke B, Montes D, Tezduyar TE, Hsu M-C, Bazilevs Y (2011) Numerical-performance studies for the stabilized space–time computation of wind-turbine rotor aerodynamics. Comput Mech 48:647–657. https://doi.org/10.1007/s00466-011-0614-5
75. Takizawa K, Tezduyar TE, McIntyre S, Kostov N, Kolesar R, Habluetzel C (2014) Space–time VMS computation of wind-turbine rotor and tower aerodynamics. Comput Mech 53:1–15. https://doi.org/10.1007/s00466-013-0888-x
76. Takizawa K, Bazilevs Y, Tezduyar TE, Hsu M-C, Øiseth O, Mathisen KM, Kostov N, McIntyre S (2014) Engineering analysis and design with ALE-VMS and space–time methods. Arch Comput Methods Eng 21:481–508. https://doi.org/10.1007/s11831-014-9113-0
77. Takizawa K (2014) Computational engineering analysis with the new-generation space–time methods. Comput Mech 54:193–211. https://doi.org/10.1007/s00466-014-0999-z
78. Korobenko A, Bazilevs Y, Takizawa K, Tezduyar TE (2018) Recent advances in ALE-VMS and ST-VMS computational aerodynamic and FSI analysis of wind turbines. In: Tezduyar TE (ed) Frontiers in computational fluid–structure interaction and flow simulation: research from lead investigators under forty—2018, Modeling and Simulation in Science, Engineering and Technology, pp 249–331. Springer, Berlin. 2018, ISBN: 978-3-319-96468-3. https://doi.org/10.1007/978-3-319-96469-0_7
79. Takizawa K, Henicke B, Puntel A, Kostov N, Tezduyar TE (2012) Space–time techniques for computational aerodynamics modeling of flapping wings of an actual locust. Comput Mech 50:743–760. https://doi.org/10.1007/s00466-012-0759-x
80. Takizawa K, Henicke B, Puntel A, Kostov N, Tezduyar TE (2013) Computer modeling techniques for flapping-wing aerodynamics of a locust. Comput Fluids 85:125–134. https://doi.org/10.1016/j.compfluid.2012.11.008
81. Takizawa K, Kostov N, Puntel A, Henicke B, Tezduyar TE (2012) Space–time computational analysis of bio-inspired flapping-wing aerodynamics of a micro aerial vehicle. Comput Mech 50:761–778. https://doi.org/10.1007/s00466-012-0758-y
82. Takizawa K, Tezduyar TE, Kostov N (2014) Sequentially-coupled space-time FSI analysis of bio-inspired flapping-wing aerodynamics of an MAV. Comput Mech 54:213–233. https://doi.org/10.1007/s00466-014-0980-x
83. Takizawa K, Tezduyar TE, Buscher A (2015) Space–time computational analysis of MAV flapping-wing aerodynamics with wing clapping. Comput Mech 55:1131–1141. https://doi.org/10.1007/s00466-014-1095-0
84. Takizawa K, Bazilevs Y, Tezduyar TE, Long CC, Marsden AL, Schjodt K (2014) ST and ALE-VMS methods for patient-specific cardiovascular fluid mechanics modeling. Math Models Methods Appl Sci 24:2437–2486. https://doi.org/10.1142/S0218202514500250
85. Takizawa K, Schjodt K, Puntel A, Kostov N, Tezduyar TE (2012) Patient-specific computer modeling of blood flow in cerebral arteries with aneurysm and stent. Comput Mech 50:675–686. https://doi.org/10.1007/s00466-012-0760-4
86. Takizawa K, Schjodt K, Puntel A, Kostov N, Tezduyar TE (2013) Patient-specific computational analysis of the influence of a stent on the unsteady flow in cerebral aneurysms. Comput Mech 51:1061–1073. https://doi.org/10.1007/s00466-012-0790-y
87. Suito H, Takizawa K, Huynh VQH, Sze D, Ueda T (2014) FSI analysis of the blood flow and geometrical characteristics in the thoracic aorta. Comput Mech 54:1035–1045. https://doi.org/10.1007/s00466-014-1017-1
88. Suito H, Takizawa K, Huynh VQH, Sze D, Ueda T, Tezduyar TE (2016) A geometrical-characteristics study in patient-specific FSI analysis of blood flow in the thoracic aorta. In: Bazilevs Y, Takizawa K (eds) Advances in computational fluid–structure interaction and flow simulation: new methods and challenging computations, modeling and simulation in science, engineering and technology, pp 379–386. Springer, Berlin. ISBN: 978-3-319-40825-5, https://doi.org/10.1007/978-3-319-40827-9_29
89. Takizawa K, Tezduyar TE, Uchikawa H, Terahara T, Sasaki T, Shiozaki K, Yoshida A, Komiya K, Inoue G (2018) Aorta flow analysis and heart valve flow and structure analysis. In: Tezduyar TE (ed) Frontiers in computational fluid–structure interaction and flow simulation: research from lead investigators under forty—2018, Modeling and simulation in science, engineering and technology, pp 29–88. Springer, Berlin. ISBN: 978-3-319-96468-3, https://doi.org/10.1007/978-3-319-96469-0_2
90. Takizawa K, Tezduyar TE, Uchikawa H, Terahara T, Sasaki T, Yoshida A (2018) Mesh refinement influence and cardiac-cycle flow periodicity in aorta flow analysis with isogeometric discretization. Comput Fluids. https://doi.org/10.1016/j.compfluid.2018.05.025
91. Takizawa K, Tezduyar TE (2016) New directions in space–time computational methods. In: Bazilevs Y and Takizawa K (eds) Advances in computational fluid–structure interaction and flow simulation: new methods and challenging computations, modeling and simulation in science, engineering and technology, pp 159–178. Springer, Springer. ISBN: 978-3-319-40825-5, https://doi.org/10.1007/978-3-319-40827-9_13
92. Takizawa K, Tezduyar TE, Terahara T, Sasaki T (2018) Heart valve flow computation with the space–time slip interface topology change (ST-SI-TC) method and isogeometric analysis (IGA). In: Wriggers P, Lenarz T (eds) Biomedical technology: modeling, experiments and simulation, Lecture Notes in Applied and Comput Mech, pp 77–99. Springer, Berlin. ISBN: 978-3-319-59547-4, https://doi.org/10.1007/978-3-319-59548-1_6
93. Takizawa K, Montes D, McIntyre S, Tezduyar TE (2013) Space-time VMS methods for modeling of incompressible flows at high Reynolds numbers. Math Models Methods Appl Sci 23:223–248. https://doi.org/10.1142/s0218202513400022
94. Takizawa K, Tezduyar TE, Hattori H (2017) Computational analysis of flow-driven string dynamics in turbomachinery. Comput Fluids 142:109–117. https://doi.org/10.1016/j.compfluid.2016.02.019
95. Komiya K, Kanai T, Otoguro Y, Kaneko M, Hirota K, Zhang Y, Takizawa K, Tezduyar TE, Nohmni M, Tsuneda T, Kawai M, Isono M (2018) Computational analysis of flow-driven string dynamics in a pump and residence time calculation. In: Proceedings of the 29th IAHR symposium on hydraulic machinery and systems, Kyoto, Japan
96. Otoguro Y, Takizawa K, Tezduyar TE (2017) Space–time VMS computational flow analysis with isogeometric discretization and a general-purpose NURBS mesh generation method. Comput Fluids 158:189–200. https://doi.org/10.1016/j.compfluid.2017.04.017
97. Otoguro Y, Takizawa K., Tezduyar T.E. (2018) A general-purpose NURBS mesh generation method for complex geometries. In: Tezduyar TE (ed) Frontiers in computational fluid–structure interaction and flow simulation: research from lead investigators under forty—2018, Modeling and simulation in science, engineering and technology, pp 395–429. Springer, Berlin. ISBN: 978-3-319-96468-3, https://doi.org/10.1007/978-3-319-96469-0_10

98. Otoguro Y, Takizawa K, Tezduyar TE, Nagaoka K, Mei S (2018) Turbocharger turbine and exhaust manifold flow computation with the space–time variational multiscale method and isogeometric analysis. Comput Fluids. https://doi.org/10.1016/j.compfluid.2018.05.019
99. Takizawa K, Tezduyar TE, Asada S, Kuraishi T (2016) Space–time method for flow computations with slip interfaces and topology changes (ST-SI-TC). Comput Fluids 141:124–134. https://doi.org/10.1016/j.compfluid.2016.05.006
100. Takizawa K, Tezduyar TE, Terahara T (2016) Ram-air parachute structural and fluid mechanics computations with the space–time isogeometric analysis (ST-IGA). Comput Fluids 141:191–200. https://doi.org/10.1016/j.compfluid.2016.05.027
101. Takizawa K, Tezduyar TE, Kanai T (2017) Porosity models and computational methods for compressible-flow aerodynamics of parachutes with geometric porosity. Math Models Methods Appl Sci 27:771–806. https://doi.org/10.1142/S0218202517500166
102. Kanai T, Takizawa K, Tezduyar TE, Tanaka T, Hartmann A (2018) Compressible-flow geometric-porosity modeling and spacecraft parachute computation with isogeometric discretization. Comput Mech. https://doi.org/10.1007/s00466-018-1595-4
103. Takizawa K, Tezduyar TE, Otoguro Y (April 2018) Stabilization and discontinuity-capturing parameters for space–time flow computations with finite element and isogeometric discretizations. Comput Mech. https://doi.org/10.1007/s00466-018-1557-x
104. Tezduyar TE, Aliabadi SK, Behr M, Mittal S (1994) Massively parallel finite element simulation of compressible and incompressible flows. Comput Methods Appl Mech Eng 119:157–177. https://doi.org/10.1016/0045-7825(94)00082-4
105. Takizawa K, Tezduyar TE (2014) Space–time computation techniques with continuous representation in time (ST-C). Comput Mech 53:91–99. https://doi.org/10.1007/s00466-013-0895-y
106. Tezduyar TE, Ganjoo DK (1986) Petrov–Galerkin formulations with weighting functions dependent upon spatial and temporal discretization: applications to transient convection-diffusion problems. Comput Methods Appl Mech Eng 59:49–71. https://doi.org/10.1016/0045-7825(86)90023-X
107. Le Beau GJ, Ray SE, Aliabadi SK, Tezduyar TE (1993) SUPG finite element computation of compressible flows with the entropy and conservation variables formulations. Comput Methods Appl Mech Eng 104:397–422. https://doi.org/10.1016/0045-7825(93)90033-T
108. Tezduyar TE (2007) Finite elements in fluids: stabilized formulations and moving boundaries and interfaces. Comput Fluids 36:191–206. https://doi.org/10.1016/j.compfluid.2005.02.011
109. Tezduyar TE, Senga M (2006) Stabilization and shock-capturing parameters in SUPG formulation of compressible flows. Comput Methods Appl Mech Eng 195:1621–1632. https://doi.org/10.1016/j.cma.2005.05.032
110. Tezduyar TE, Senga M (2007) SUPG finite element computation of inviscid supersonic flows with YZβ shock-capturing. Comput Fluids 36:147–159. https://doi.org/10.1016/j.compfluid.2005.07.009
111. Tezduyar TE, Senga M, Vicker D (2006) Computation of inviscid supersonic flows around cylinders and spheres with the SUPG formulation and YZβ shock-capturing. Comput Mech 38:469–481. https://doi.org/10.1007/s00466-005-0025-6
112. Tezduyar TE, Sathe S (2006) Enhanced-discretization selective stabilization procedure (EDSSP). Comput Mech 38:456–468. https://doi.org/10.1007/s00466-006-0056-7
113. Corsini A, Rispoli F, Santoriello A, Tezduyar TE (2006) Improved discontinuity-capturing finite element techniques for reaction effects in turbulence computation. Comput Mech 38:356–364. https://doi.org/10.1007/s00466-006-0045-x
114. Rispoli F, Corsini A, Tezduyar TE (2007) Finite element computation of turbulent flows with the discontinuity-capturing directional dissipation (DCDD). Comput Fluids 36:121–126. https://doi.org/10.1016/j.compfluid.2005.07.004
115. Tezduyar TE, Ramakrishnan S, Sathe S (2008) Stabilized formulations for incompressible flows with thermal coupling. Int J Numer Methods Fluids 57:1189–1209. https://doi.org/10.1002/fld.1743
116. Rispoli F, Saavedra R, Corsini A, Tezduyar TE (2007) Computation of inviscid compressible flows with the V-SGS stabilization and YZβ shock-capturing. Int J Numer Methods Fluids 54:695–706. https://doi.org/10.1002/fld.1447
117. Bazilevs Y, Calo VM, Tezduyar TE, Hughes TJR (2007) YZβ discontinuity-capturing for advection-dominated processes with application to arterial drug delivery. Int J Numer Methods Fluids 54:593–608. https://doi.org/10.1002/fld.1484
118. Corsini A, Menichini C, Rispoli F, Santoriello A, Tezduyar TE (2009) A multiscale finite element formulation with discontinuity capturing for turbulence models with dominant reactionlike terms. J Appl Mech 76:021211. https://doi.org/10.1115/1.3062967
119. Rispoli F, Saavedra R, Menichini F, Tezduyar TE (2009) Computation of inviscid supersonic flows around cylinders and spheres with the V-SGS stabilization and YZβ shock-capturing. J Appl Mech 76:021209. https://doi.org/10.1115/1.3057496
120. Corsini A, Iossa C, Rispoli F, Tezduyar TE (2010) A DRD finite element formulation for computing turbulent reacting flows in gas turbine combustors. Comput Mech 46:159–167. https://doi.org/10.1007/s00466-009-0441-0
121. Hsu M-C, Bazilevs Y, Calo VM, Tezduyar TE, Hughes TJR (2010) Improving stability of stabilized and multiscale formulations in flow simulations at small time steps. Comput Methods Appl Mech Eng 199:828–840. https://doi.org/10.1016/j.cma.2009.06.019
122. Corsini A, Rispoli F, Tezduyar TE (2011) Stabilized finite element computation of NOx emission in aero-engine combustors. Int J Numer Methods Fluids 65:254–270. https://doi.org/10.1002/fld.2451
123. Corsini A, Rispoli F, Tezduyar TE (2012) Computer modeling of wave-energy air turbines with the SUPG/PSPG formulation and discontinuity-capturing technique. J Appl Mech 79:010910. https://doi.org/10.1115/1.4005060
124. Corsini A, Rispoli F, Sheard AG, Tezduyar TE (2012) Computational analysis of noise reduction devices in axial fans with stabilized finite element formulations. Comput Mech 50:695–705. https://doi.org/10.1007/s00466-012-0789-4
125. Kler PA, Dalcin LD, Paz RR, Tezduyar TE (2013) SUPG and discontinuity-capturing methods for coupled fluid mechanics and electrochemical transport problems. Comput Mech 51:171–185. https://doi.org/10.1007/s00466-012-0712-z
126. Corsini A, Rispoli F, Sheard AG, Takizawa K, Tezduyar TE, Venturini P (2014) A variational multiscale method for particle-cloud tracking in turbomachinery flows. Comput Mech 54:1191–1202. https://doi.org/10.1007/s00466-014-1050-0

127. Rispoli F, Delibra G, Venturini P, Corsini A, Saavedra R, Tezduyar TE (2015) Particle tracking and particle-shock interaction in compressible-flow computations with the V-SGS stabilization and YZβ shock-capturing. Comput Mech 55:1201–1209. https://doi.org/10.1007/s00466-015-1160-3

128. Saad Y, Schultz M (1986) GMRES: a generalized minimal residual algorithm for solving nonsymmetric linear systems. SIAM J Sci Stat Comput 7:856–869